

Dynamically-enhanced strain in atomically thin resonators

Xin Zhang,^{1,*} Kevin Makles,¹ Léo Colombier,¹ Dominik Metten,¹
Hicham Majjad,¹ Pierre Verlot,^{2,3} and Stéphane Berciaud^{1,3,†}

¹*Université de Strasbourg, CNRS, Institut de Physique et Chimie des
Matériaux de Strasbourg, UMR 7504, F-67000 Strasbourg, France*

²*School of Physics and Astronomy, University of Nottingham, Nottingham, NG7 2RD, United Kingdom*

³*Institut Universitaire de France, 1 rue Descartes, 75231 Paris cedex 05, France*

Owing to their low mass and outstanding mechanical figures of merit, graphene and related two-dimensional (2D) materials are ideal building blocks for nano-electro-mechanical systems. At the same time, 2D materials are endowed with unique electronic, optical and phononic properties, suitable for hybrid systems that couple their elementary excitations (excitons, phonons) and/or degrees of freedom (spin, valley) to macroscopic flexural vibrations. The built-in nature of such hybrid systems may yield enhanced strain-mediated coupling as compared to bulkier hybrid systems, e.g., comprising a single quantum emitter coupled to a nano-mechanical resonator. Here, using micro-Raman scattering spectroscopy on circular drums made from pristine graphene monolayers, we demonstrate dynamical softening of optical phonons induced by the macroscopic flexural motion of graphene. This softening is an unambiguous fingerprint of dynamically-induced tensile strain that reaches values up to $\approx 4 \times 10^{-4}$ under strong non-linear driving. These anomalously large strains exceed the time-averaged values predicted for harmonic vibrations with the same root mean square (RMS) amplitude by more than one order of magnitude and are proportional to the non-linear frequency shift of the mechanical resonance of the drum. Our work provides an impetus for modelling non-linear dynamics in atomically thin resonators beyond elasticity theory and holds promise for dynamical strain engineering and dynamical strain-mediated control of light-matter interactions, single-photon emission or magnetic order in 2D materials and related heterostructures.

Since the first demonstration of mechanical resonators made from suspended graphene layers¹, considerable progress has been made to conceive nano-mechanical systems based on 2D materials^{2,3} with well-characterized performances⁴⁻⁸, for applications in mass and force sensing⁹ but also for studies of heat transport^{10,11}, non-linear mode coupling¹²⁻¹⁴ and optomechanical interactions^{5,15,16}. These efforts triggered the study of 2D resonators beyond graphene, made for instance from transition metal dichalcogenide layers^{8,11,17,18} and van der Waals heterostructures¹⁹⁻²¹. In suspended atomically thin membranes, a moderate out-of-plane stress gives rise to large and swiftly tunable strains, in excess of 1%^{22,23}, opening numerous possibilities for strain-engineering²⁴. These assets also position 2D materials as promising systems to achieve enhanced strain-mediated coupling²⁵⁻²⁸ of macroscopic flexural vibrations to quasiparticles (excitons, phonons) and/or degrees of freedom (spin, valley). Such developments require sensitive probes of dynamical strain. Among the approaches employed to characterise strain in 2D materials, micro-Raman scattering spectroscopy²⁹ stands out as a local, contactless and minimally invasive technique that has been extensively exploited in the static regime to quantitatively convert the frequency softening or hardening of the Raman active modes into an amount of tensile or compressive strain, respectively³⁰⁻³³. Although dynamically-induced strain has been investigated using Raman spectroscopy in bulkier micro electro-mechanical systems^{34,35}, including mesoscopic graphite cantilevers³⁶, it remains unexplored in resonators made from 2D materials.

In this article, using micro-Raman scattering spec-

troscopy in 2D resonators made from pristine suspended graphene monolayers, we demonstrate efficient strain-mediated coupling between “built-in” quantum degrees of freedom (here the Raman-active optical phonons of graphene) of the 2D resonator, and its macroscopic flexural vibrations. The dynamically-induced strain is quantitatively determined from the frequency of the Raman-active modes and are found to be anomalously large, exceeding the levels of strain achievable in the static regime by more than one order of magnitude. Our work introduces resonators made from graphene and related 2D materials as unique atomically thin opto-electro-mechanical systems³⁷, promising for hybrid optomechanics and dynamical strain-mediated control of their rich light-matter interactions.

Results

Measurement Scheme – As illustrated in Fig. 1a, the system we have developed for probing dynamical strain in the 2D limit is a monolayer graphene drum deposited onto a pre-patterned Si/SiO₂ substrate and capacitively driven using a time-dependent gate bias $V_g(t) = V_{dc} + V_{ac} \cos \Omega t$, with $V_{ac} \ll V_{dc}$ and $\Omega/2\pi$ the drive frequency. The DC component of the resulting force ($\propto V_g^2$, see Methods) enables to control the electrostatic pressure applied to the graphene membrane (and hence its static deflection ξ , see Fig. 1a), whereas the AC bias leads to a harmonic driving force ($\propto V_{dc} V_{ac} \cos \Omega t$). A single laser beam is used to interferometrically measure the frequency-dependent mechanical susceptibility at the drive frequency, akin to Ref. 1 and, at the same time, to record the micro-Raman scattering response of the atomically thin membrane. All measurements were performed

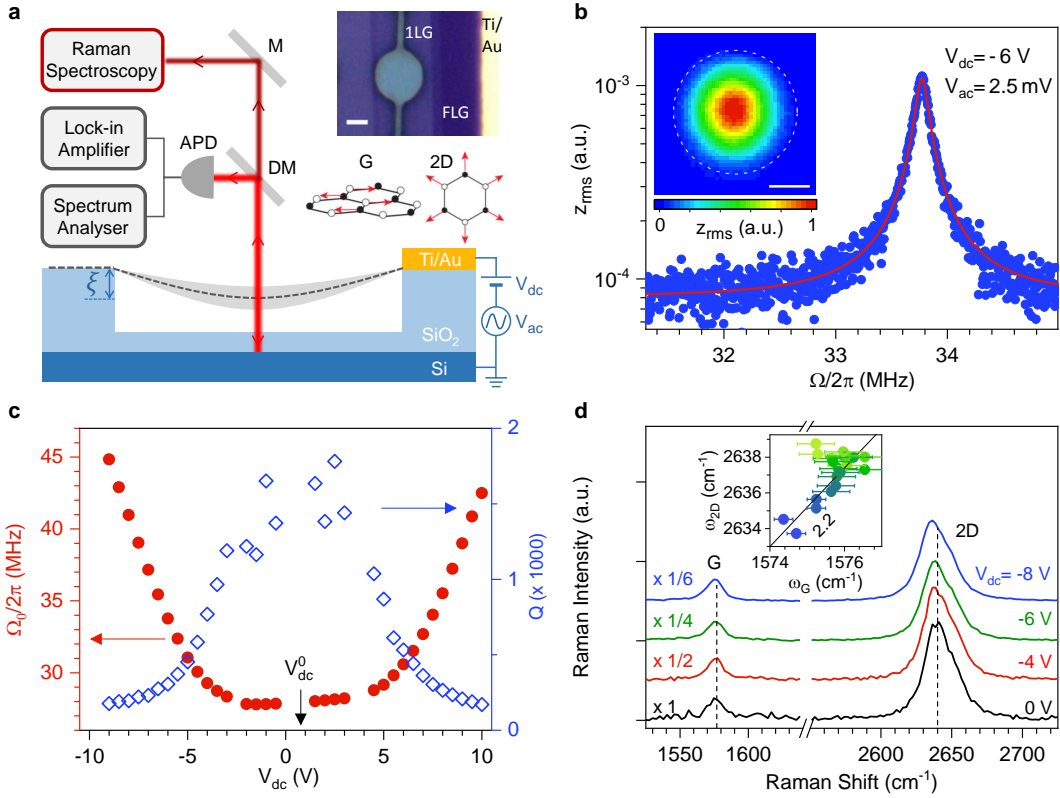


FIG. 1. **Experimental setup and characterisation of pristine graphene drums.** **a**, Sketch of our experiment combining electrostatic actuation, optical readout of the displacement and micro-Raman spectroscopy of a circular graphene drum (device 1). The graphene layer (with its static displacement ξ) is represented by the dark grey dashed line; its flexural motion is sketched with the light grey shade. M, DM, APD represent a mirror, a dichroic mirror, an avalanche photodiode, respectively. Upper inset: optical image of a suspended graphene monolayer (1L) contacted by a Ti/Au lead (scale bar: $2 \mu\text{m}$). A thicker, few-layer graphene flake (FLG) is also visible. Lower inset: sketch of the atomic displacements contributing to the Raman G mode and 2D mode. **b**, RMS mechanical amplitude z_{rms} (blue dots) as a function of the drive frequency $\Omega/2\pi$ at $V_{\text{dc}} = -6 \text{ V}$ and $V_{\text{ac}} = 2.5 \text{ mV}$. The red line is a fit based on linear response theory (Supplementary Section 6). Inset: map of the resonant mechanical (scale bar: $2 \mu\text{m}$). **c**, Resonance frequency $\Omega_0/2\pi$ and corresponding quality factor Q as a function of V_{dc} , with V_{dc}^0 indicating the charge neutrality point in graphene. **d**, Raman spectra measured at the centre of the drum at $V_{\text{dc}} = 0, -4, -6, -8 \text{ V}$ and $V_{\text{ac}} = 0 \text{ mV}$. Inset: correlation between the G- and 2D-mode frequencies (ω_{2D} and ω_G), extracted from Raman spectra measured with V_{dc} varying from -9 V to 10 V . The light green-to-blue color scale in circles encodes the increase of $|V_{\text{dc}} - V_{\text{dc}}^0|$. The straight black line with a slope of 2.2 is a guide to the eye corresponding to strain-induced phonon softening.

at room temperature under high vacuum (see Methods and Supplementary Sections 1 to 7).

Raman spectroscopy in strained graphene – The Raman spectrum of graphene displays two main features: the G mode and the 2D mode, arising from one zone-center (that is, zero momentum) phonon and from a pair of near-zone edge phonons with opposite momenta, respectively (see Fig. 1a and Supplementary Section 1)²⁹. Both features are uniquely sensitive to external perturbations. Quantitative methods have been developed to unambiguously separate the share of strain, doping, and possibly heating effects that affect the frequency, full width at half maximum (FWHM) and integrated intensity of a Raman feature^{31,38–41} (hereafter denoted ω_i , Γ_i , I_i , respectively, here with $i = \text{G}, 2D$). Biaxial

strain is expected around the centre of circular graphene drums²² and the large Grüneisen parameters of graphene ($\gamma_{\text{G}} = 1.8$ and $\gamma_{2D} = 2.4$, with $\gamma_i = \frac{1}{2\omega_i} \frac{\partial \omega_i}{\partial \varepsilon}$ and ε the level of biaxial strain)^{31,32} allow detection of strain levels down to a few 10^{-5} . The characteristic slope $\frac{\partial \omega_{2D}}{\partial \omega_{\text{G}}} \approx 2.2$ in graphene under biaxial strain is much larger than in the case of electron or hole doping, where the corresponding slope is significantly smaller than 1^{39,40}.

Mechanical and Raman characterisation – Figure 1b presents the main characteristics of a circular graphene drum (device 1) in the linear response regime. A Lorentzian mechanical resonance is observed at $\Omega_0/2\pi \approx 33.8 \text{ MHz}$ for $V_{\text{dc}} = -6 \text{ V}$ (Fig. 1b and Supplementary Sections 5 and 6). The mechanical mode profile shows radial symmetry (inset in Fig. 1b) as ex-

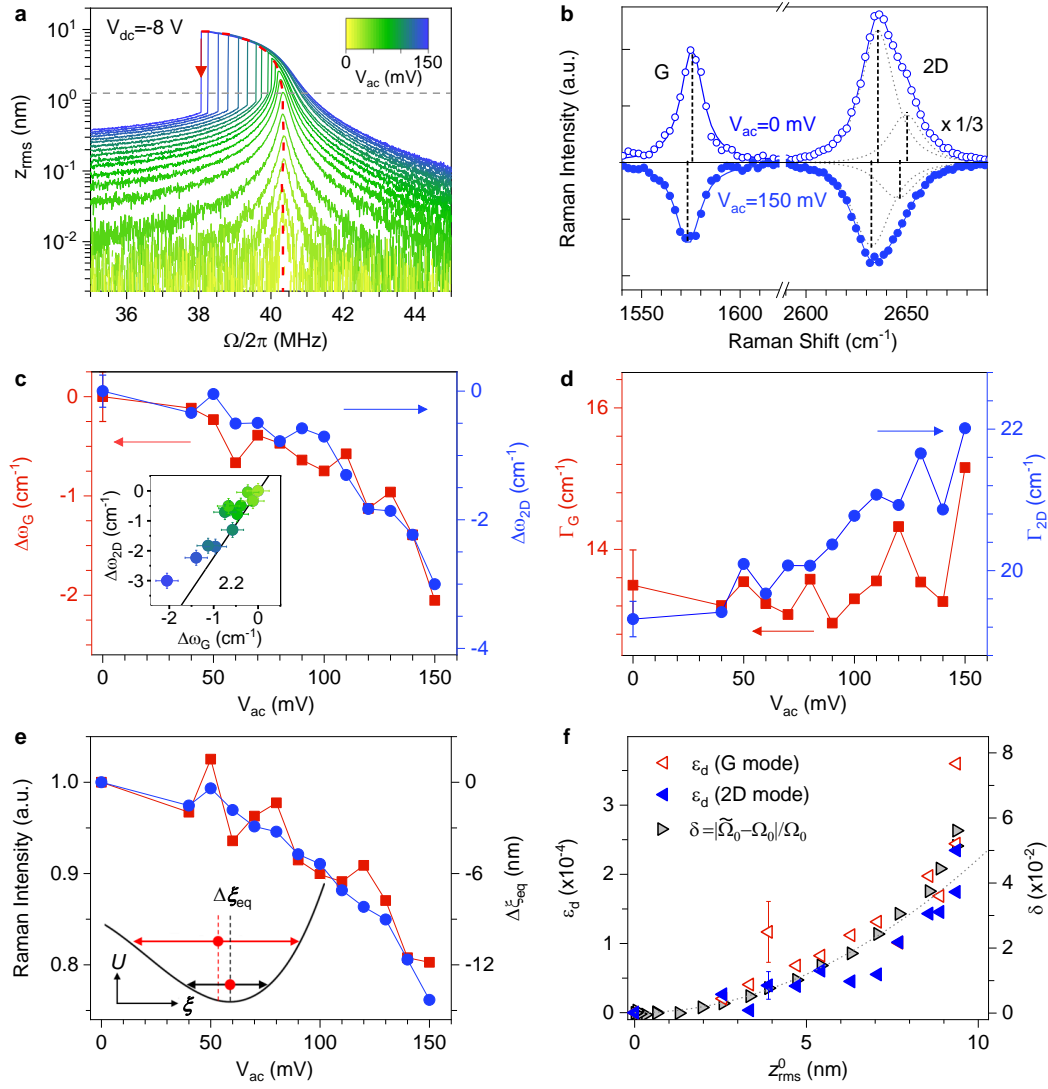


FIG. 2. Evidence for dynamically-enhanced strain in graphene. All measurements are performed on device 1 at $V_{dc} = -8$ V. **a**, Calibrated RMS mechanical amplitude at the drive frequency $\Omega/2\pi$ (z_{rms}) recorded as the frequency is swept downwards, for V_{ac} increasing from 0 to 150 mV. The red dashed line is the backbone curve evidencing non-linear resonance frequency softening. The red arrow indicates the jump-down frequency at $V_{ac} = 150$ mV. The grey dashed line denotes the onset of non-linearity. **b**, Raman spectra measured under $V_{ac} = 0$ mV (open symbols and fit) and 150 mV (filled symbols and fit, vertically flipped for clarity). **c,d**, G- and 2D-mode frequency shifts $\Delta\omega_{G,2D}$ and full-width at half maximum variations ($\Delta\Gamma_{G,2D}$), relative to the values at $V_{ac} = 0$ mV, as a function of V_{ac} . Inset in **c**: correlation between $\Delta\omega_{2D}$ and $\Delta\omega_G$. The symbol color encodes the increase of V_{ac} as in **a**. The straight black line with a slope of 2.2 is a guide to the eye for strain-induced phonon softening. **e**, Normalized integrated intensity of G- and 2D-mode features as a function of V_{ac} . The inset illustrates the equilibrium position shift ($\Delta\xi_{eq}$ between the two red circles) in the non-linear regime, with $U(\xi)$ the potential energy. **f**, Time-averaged dynamical strain ε_d extracted from the softening of G- and 2D-mode features (open red and filled blue triangles, respectively) as a function of the corresponding z_{rms}^0 . The right axis (grey triangles) shows the relative non-linear mechanical resonance frequency shift $\delta = |\tilde{\Omega}_0 - \Omega_0|/\Omega_0$, where $\tilde{\Omega}_0$ is the jump-down frequency in **a**. The grey dashed line is a parabolic fit (Supplementary Section 6b). Error bars in **c,d,f** are extracted from the fits of Raman spectra. Only one error bar is included in each plot for visibility.

pected for the fundamental flexural resonance of a circular drum⁶. The mechanical resonance frequency is widely gate-tunable: it increases by $\sim 70\%$ as $|V_{dc}|$ is ramped up to 10 V and displays a symmetric, “U-shaped” behavior with respect to $V_{dc}^0 = 0.75$ V, where

graphene is charge neutral. These two features are characteristic of a low built-in tension^{4,8,10,42} that we estimate to be $T_0 = (4 \pm 0.4) \times 10^{-2} \text{ Nm}^{-1}$, that is a built-in static strain $\varepsilon_s^0 = T_0(1 - \nu^2)/E_{1LG} \approx (1.1 \pm 0.1) \times 10^{-4}$, where $E_{1LG} = 340 \text{ N m}^{-1}$, $\nu = 0.16$ are the Young mod-

ulus and Poisson ratio of pristine monolayer graphene⁴³ (Supplementary Section 6). The quality factor Q is high, in excess of 1500 near charge neutrality. As $|V_{\text{dc}}|$ increases, Q drops down to ~ 200 due to electrostatic damping⁸.

Figure 1d shows that the Raman response of suspended graphene is tunable by application of a DC gate bias, as discussed in Ref. 41. Once V_{dc} is large enough to overcome ε_s^0 , the membrane starts to bend downwards and the downshifts of the G- and 2D-mode features measured at the centre of the drum are chiefly due to biaxial strain ($\partial\omega_G/\partial\omega_{2D} \approx 2.2$, see inset in Fig. 1d) with negligible contribution from electrostatic doping⁴¹. At $V_{\text{dc}} = -9$ V, the 4 ± 0.5 cm⁻¹ 2D-mode downshift relative to its value near V_{dc}^0 yields a gate-induced static strain $\varepsilon_s = 3 \pm 0.3 \times 10^{-4}$ that agrees qualitatively well with the value $\varepsilon_s = 2 \pm 0.2 \times 10^{-4}$ estimated from the gate-induced upshift of Ω_0 (Fig. 1c and Supplementary Section 6). This agreement justifies our assumption that the Young modulus of our drum is close to that of pristine graphene (see also Supplementary Section 5 for details on the drum effective mass).

Noteworthy, optical interference effects cause a large gate-dependent modulation of I_G and I_{2D} (Ref. 31 and 41 and see normalisation factors in Fig. 1d). Both strain-induced Raman shifts and Raman scattering intensity changes are exploited to consistently estimate that ξ increases from about 30 nm to 70 nm when V_{dc} is varied from -5 V to -9 V (Supplementary Sections 2, 3 and 4).

Non-linear mechanical response – We are now examining how the dynamically-induced strain can be readout by means of Raman spectroscopy. First, to obtain a larger sensitivity towards static strain (Supplementary Section 3), we apply a sufficiently high V_{dc} to reach a sizeable ξ . V_{ac} is then ramped up to yield large RMS amplitudes. After calibration of our setup (Supplementary Section 5), we estimate that resonant RMS amplitudes z_{rms}^0 up to ~ 10 nm are attained in device 1 (Fig. 2,3). In this regime, graphene is a strongly non-linear mechanical system that can be described to lowest order by a Duffing-like equation^{5,7,44}:

$$\ddot{z} + \frac{\Omega_0}{Q}\dot{z} + \Omega_0^2 z + \tilde{\alpha}_3 z^3 = \frac{\tilde{F}_{el}}{\tilde{m}} \cos(\Omega t), \quad (1)$$

where z is the mechanical displacement at the membrane center relative to the equilibrium position ξ , $\Omega_0/2\pi$ is the resonance frequency in the linear regime, Q is the quality factor and Ω_0/Q is the linear damping rate. The effective mass and effective applied electrostatic force \tilde{F}_{el} account for the mode shape of the fundamental resonance in a rigidly clamped circular drum^{6,45} (see Methods and Supplementary Section 6). The linear spring constant is $\tilde{m}\Omega_0^2$. Mechanical non-linearities are considered using an effective third-order term $\tilde{\alpha}_3$ that changes sign at large enough ξ , leading to a transition from non-linear hardening to non-linear softening⁵. Such a behaviour is indeed revealed in our experiments, as shown

in Fig. 2a and Fig.3a, where non-linear softening and non-linear hardening are observed at $V_{\text{dc}} = -8$ V and $V_{\text{dc}} = -6$ V, respectively. At $V_{\text{dc}} = -7$ V, we observe a V_{ac} -dependent softening-to-hardening transition (Supplementary Sections 6 and 8).

Dynamical optical phonon softening – Figure 2c-e shows the frequencies, linewidths and integrated intensities of the Raman features measured at $V_{\text{dc}} = -8$ V (where $\xi \approx 60$ nm), with V_{ac} increasing from 0 to 150 mV and applied at a drive frequency that tracks the V_{ac} -dependent non-linear softening of the mechanical resonance frequency $\tilde{\Omega}_0/2\pi$, that is the so-called backbone curve in Fig. 2a,f (Supplementary Section 6). Both G- and 2D-mode features downshift as the drum is non-linearly driven. This phonon softening is accompanied by spectral broadening by up to $\sim 10 - 15$ % (Fig. 2d). The correlation plot between ω_{2D} and ω_G reveals a linear slope near 2, which is a characteristic signature of tensile strain^{31,39} that gets as high as $\approx 2.5 \times 10^{-4}$ for $z_{\text{rms}} \approx 9$ nm.

In Fig. 3a, we compare, on device 1, the frequency-dependence of z_{rms} to that of $\omega_{G,2D}$ and I_{2D} , for upward and downward sweeps under $V_{\text{dc}} = -6$ V and $V_{\text{ac}} = 100$ mV. As in Fig. 2c, sizeable G-mode and 2D-mode softening is observed near the mechanical resonance (Fig. 3a-c) and assigned to tensile strain (see correlation plot in Fig. 3c). Remarkably, the hysteretic behavior of the mechanical susceptibility, associated with non-linear hardening at $V_{\text{dc}} = -6$ V, is well-imprinted onto the frequency-dependence of $\omega_{G,2D}$ and I_{2D} . Looking further at Fig. 3a, we notice that while z_{rms} fully saturates at drive frequencies above 33.5 MHz and ultimately starts to decrease near the jump-down frequency, the tensile strain keeps increasing linearly up to $\approx 2.5 \times 10^{-4}$ as $\Omega/2\pi$ is raised from 33.2 MHz up to 34.5 MHz.

Equilibrium position shift – As our graphene drums are non-linearly driven, including beyond the Duffing regime (Fig. 3a and Supplementary Section 6), the large strains revealed in Fig. 2 and 3 could in part arise from an equilibrium position shift $\Delta\xi_{\text{eq}}$ due to symmetry breaking non-linearities^{44,46} (inset in Fig. 2e). This effect can be quantitatively assessed through analysis of $I_{G,2D}$. As shown in Fig. 2e both I_{2D} and I_G decrease by about ~ 20 % as V_{ac} increases up to 150 mV. These variations are assigned to optical interference effects (Ref. 31 and 41); in our experimental geometry they indicate an equilibrium position upshift $\Delta\xi_{\text{eq}}$ by up to ≈ 12 nm (Fig. 2e and Supplementary Section 4), that leads to a reduction of the static tensile strain $\Delta\varepsilon_s \approx 1 \times 10^{-4}$, in stark contrast with the *enhanced* tensile strain unambiguously revealed in Fig. 2c. Similarly, the ≈ 10 % drop in I_{2D} near the jump-down frequency at 34.5 MHz indicates an equilibrium position upshift $\Delta\xi_{\text{eq}} \approx 4$ nm that is qualitatively similar to the results in Fig. 2e. The larger $\Delta\xi_{\text{eq}}$ measured at $V_{\text{dc}} = -8$ V is consistent with our observation of non-linear mechanical resonance softening (Fig. 2a) due to an increased contribution from symmetry breaking non-linearities at large ξ

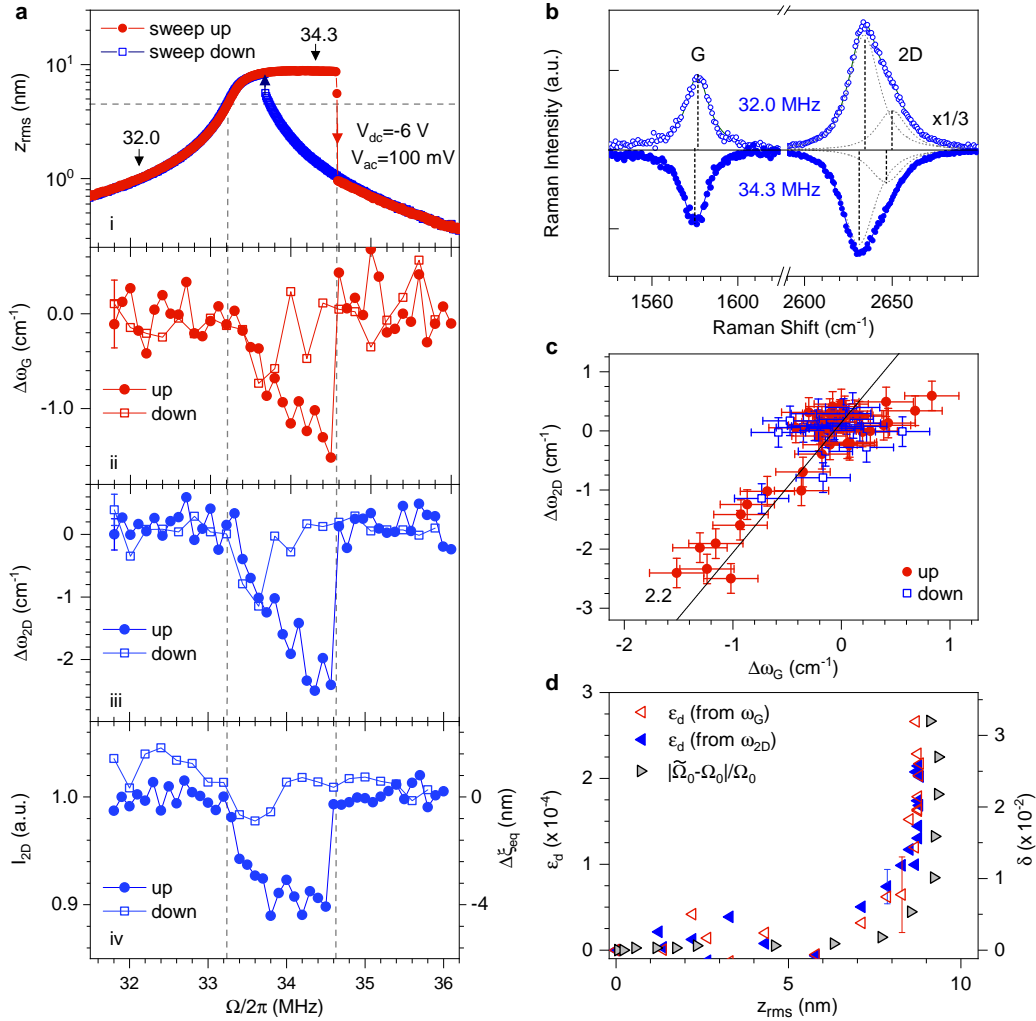


FIG. 3. Frequency-dependent dynamically-induced strain. All measurements are performed on device 1 under $V_{dc} = -6$ V **a**, Panel i: Mechanical amplitude z as a function of the drive frequency $\Omega/2\pi$ under $V_{ac} = 100$ mV. Red filled circles and blue open squares indicate upward and downward frequency sweeps. The blue and red arrows denote the jump-down and jump-up frequencies in the non-linear hardening region, respectively. The dashed lines are guides to the eye. Panels ii and iii: Raman frequency shifts $\Delta\omega_G$ and $\Delta\omega_{2D}$ as a function of $\Omega/2\pi$. Panel iv: Integrated intensity of the 2D-mode feature as a function of $\Omega/2\pi$. Filled and open symbols in panels 2-4 correspond to upward and downward frequency sweeps, respectively. **b**, Raman spectra recorded at $\Omega/2\pi = 32$ MHz (open symbols and fit) and 34.3 MHz (filled symbols and fit, vertically flipped for clarity), see arrows in **a**. **c** Correlation between the frequency shifts $\Delta\omega_G$ and $\Delta\omega_{2D}$, relative to the values recorded away from the mechanical resonance. The straight black line with a slope of 2.2 is a guide to the eye for the strain-induced phonon softening. **d**, Time-averaged dynamical strain ε_d extracted from the softening of G- and 2D-mode features in **aii** and **aiii** (open red and filled blue triangles, respectively) as a function of the RMS amplitude z_{rms} . The right axis (grey triangles) shows the relative non-linear mechanical resonance frequency shift $\delta = |\tilde{\Omega}_0 - \Omega_0|/\Omega_0$, where $\tilde{\Omega}_0$ is the jump-down frequency (see **a** and Supplementary Section 6b). Error bars in **a,c,d** are extracted from the fits of Raman spectra. Only one error bar is included in **a** and **d** for visibility.

(Ref. 5, 44, and 46 and Supplementary Section 6).

Evidence for dynamically-induced strain – We therefore conclude that the tensile strain measured in device 1 is dynamically-induced (hereafter denoted ε_d) and arises from the time-averaged resonant vibrations of the graphene drum. Starting from a reference recorded at

$V_{dc} = -8$ V and $V_{ac} = 0$ mV, ε_d recorded under resonant driving at $V_{ac} = 150$ mV (where $z_{rms} \approx 9$ nm) is as high as the static strain ε_s induced when ramping V_{dc} from 0 V to -8 V (where $\xi \approx 60$ nm). Along these lines, the small yet observable broadenings $\Delta\Gamma_{G,2D}$ of the Raman features (Fig. 2d) can be assigned to time-averaged Raman

frequency shifts due to dynamical strain⁴⁷. Complementary and consistent results are reported in Supplementary Section 8 for device 1 and in Supplementary Sections 9 and 10 for other graphene drums with similar designs, denoted devices 2 and 3, respectively. In device 3, we have measured ε_d up to $\approx 4 \times 10^{-4}$ for $z_{\text{rms}} \approx 14$ nm.

Spatially-resolved dynamically-induced strain – Interestingly, our diffraction-limited Raman readout enables local mapping of ε_d . Fig. 4 compares ω_{2D} and I_{2D} recorded across the diameter of a graphene drum (device 2, akin to device 1) under $V_{\text{dc}} = -6$ V with and without resonant driving. Very similar results are observed when performing a line-scan along the perpendicular direction (Supplementary Section 9). In the undriven case, we find a nearly flat ω_{2D} profile, which is consistent with the difficulty in resolving low-levels of static strain below 1×10^{-4} . In contrast, finite ε_d (Fig. 4b) and equilibrium position upshift (Fig. 4c) are observed at the centre of the drum, as in Fig. 2 and Fig. 3. We find that ε_d and the equilibrium position upshift decrease as they are probed away from the centre of the drum and the spatial profile of ε_d resembles the static tensile strain profile measured on bulged graphene blisters, where strain is biaxial at the centre of the drum and radial at the edges⁴⁸.

Dynamically-enhanced strain – It is instructive to compare the measured ε_d to $\varepsilon_d^h = 2/3(z_{\text{rms}}/a)^2$, with a the drum radius, the time-averaged dynamically-induced strain expected for an harmonic oscillation with an RMS amplitude z_{rms} (Supplementary Section 3). For the largest $z_{\text{rms}} \approx 9$ nm attained in device 1, $\varepsilon_d^h \approx 6 \times 10^{-6}$, i.e., about 40 times smaller than the measured ε_d (Fig. 2f and Fig. 3d). Under strong non-linear driving, we expect sizeable Fourier components of the mechanical amplitude at harmonics of the drive frequency, which could in part be responsible for the large discrepancy between ε_d and ε_d^h . Harmonics are indeed observed experimentally in the displacement power spectrum of our drums (Supplementary Section 9, device 2) but display amplitudes significantly smaller than the linear component at the drive frequency. In addition, we do not observe any measurable fingerprint of internal resonances^{12–14} in the displacement power spectrum.

To get further insights into the unexpectedly large ε_d deduced from the G- and 2D-mode downshifts we plot ε_d as a function of the corresponding z_{rms} at the centre of the drum (Fig. 2f and Fig. 3d). This plot is directly compared to the backbone curves that connect the resonant z_{rms} to the non-linear relative resonance frequency shift $\delta = |\tilde{\Omega}_0 - \Omega_0|/\Omega_0$, where $\tilde{\Omega}_0$ is considered equal to the measured jump-down frequency (Fig. 2a, 3a and Supplementary Section 6). Remarkably, ε_d grows proportionally to δ , both in the case of non-linear softening and hardening, including when z_{rms} fully saturates (Fig. 3). This result indicates that the enhancement of ε_d originates from the strong non-linear driving of the graphene drum and that δ can be regarded as an indirect measurement of ε_d .

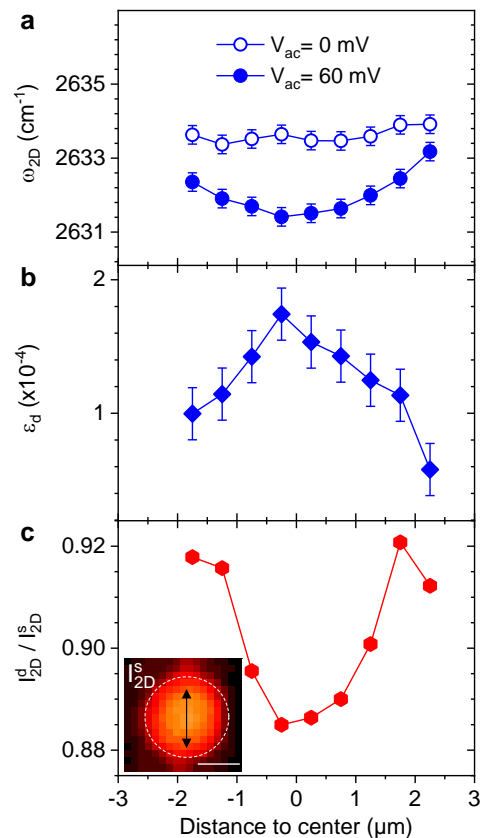


FIG. 4. **Mapping dynamically-induced strain.** **a**, Frequency of the Raman 2D mode along the cross-sections highlighted in **c** in a graphene drum (device 2, 3 μm radius) at $V_{\text{dc}} = -6$ V and $V_{\text{ac}} = 0$ mV (open symbols) and $V_{\text{ac}} = 60$ mV (full symbols). **b**, Dynamical strain ε_d obtained from the difference of the data in **a**. **c**, Ratio of the Raman 2D-mode intensity in the driven (I_{2D}^d) and static (I_{2D}^s) cases. Inset: Map of the Raman 2D-mode intensity I_{2D}^s recorded on the graphene drum (see white dashed contour), at $V_{\text{dc}} = -6$ V and $V_{\text{ac}} = 0$ V. The double arrow indicates the location of the line scan. The scale bar is 3 μm .

Discussion

The large values of $\varepsilon_d \gg \varepsilon_d^h$ reported in Fig. 2-4 cannot be understood as a purely geometrical effect arising from a smooth deflection profile of graphene over a length scale close to the drum diameter. The enhancement of ε_d could arise from so-called localization of harmonics, a phenomenon recently observed in larger and thicker (~ 500 μm wide, ~ 500 nm thick) SiN membranes⁴⁹ showing non-linear frequency-dependent mechanical susceptibility similar to Fig. 3a. In these conditions, the mechanical displacements associated with different harmonics of the drive frequency were shown to have distinct spatial profiles, possibly resulting in localized strain fields. Combining multi-mode opto-mechanical tomography and hyperspectral Raman mapping on larger graphene drums (effectively leading to a higher spatial resolution) would allow us to test whether localisation of harmonics occurs

in graphene and to possibly correlate this phenomenon to the dynamically-induced strain field. More generally, unravelling the origin of the anomalously large ε_d may require microscopic models that go beyond elasticity theory⁵⁰ and explicitly take into account the ultimate thinness and atomic structure of graphene^{51,52}.

Concluding, we have unveiled efficient coupling between intrinsic microscopic degrees of freedom (here optical phonons) and macroscopic non-linear mechanical vibrations in monolayer graphene resonators. Room temperature resonant mechanical displacement on the order of 10 nm induce unexpectedly large time-averaged dynamically-induced tensile strains up to $\approx 4 \times 10^{-4}$. Realistic improvements of our setup, including phase-resolved Raman measurements³⁵ should permit to probe dynamical strain in finer detail, including in the linear regime, where the effective coupling strength²⁸ could be extracted. For this purpose, larger resonant displacements can be achieved at cryogenic temperatures. In addition, graphene drums, as a prototypical non-linear mechanical systems, can be engineered to favor mode coupling and frequency mixing, which in return can be readout through distinct modifications of their spatially-resolved Raman scattering response.

Our approach can be directly applied to a variety of 2D materials and related van der Waals heterostructures. In few-layer systems, rigid layer shear and breathing Raman-active modes^{29,33} could be used as invaluable probes of in-plane and out-of-plane dynamical strain, respectively. Strain-mediated coupling could also be employed to manipulate the rich excitonic manifolds in transition metal dichalcogenides⁵³ as well as the single photon emitters they can host^{54,55}. More broadly, light absorption and emission could be controlled electro-mechanically in nanoresonators made from custom-designed van der Waals heterostructures⁵⁶. Going one step further, with the emergence of 2D materials featuring robust magnetic order and topological phases⁵⁷, that can be probed using optical spectroscopy, we foresee new possibilities to explore and harness phase transitions using nanomechanical resonators based on 2D materials^{58,59}.

Methods

Device fabrication – Monolayer graphene flakes were deposited onto pre-patterned 285nm-SiO₂/Si substrates, using a thermally assisted mechanical exfoliation scheme as in Ref. 60. The pattern is created by optical lithography followed by reactive ion etching and consists of hole arrays (5 and 6 μm in diameter and 250 ± 5 nm in depth) connected by ~ 1 μm -wide venting channels. Ti(3 nm)/Au(47 nm) contacts are evaporated using a transmission electron microscopy grid as a shadow mask⁴¹ to avoid any contamination with resists and solvents. With this method, we could routinely obtain pristine monolayer graphene resonators with quality factors in excess of 1,500 at room temperature in high vacuum.

Optomechanical measurements – Electrically connected graphene drums are mounted into a vacuum chamber (5×10^{-5} mbar). The drums are capacitively driven using the Si wafer as a backgate and a time-dependent gate bias $V_g(t) = V_{dc} + V_{ac} \cos \Omega t$ is applied as indicated in the main text. The applied force is given by $\epsilon_0 \pi a^2 \frac{V_g^2(t)}{2d^2(\xi)}$, where a is the drum radius, ϵ_0 the vacuum dielectric constant, $d(\xi) = (d_{vac} - \xi) + d_{SiO_2}/\epsilon_{SiO_2}$ the effective distance between graphene and the Si substrate, with ξ the static displacement, d_{vac} the graphene-SiO₂ distance in the absence of any gate bias, d_{SiO_2} the thickness of the residual SiO₂ layer. This force contains a static component proportional to V_{dc}^2 , which sets the value of ξ and a harmonic driving force proportional to $V_{dc} V_{ac} \cos(\Omega t)$. Note that since $V_{ac} \ll |V_{dc}|$, we can safely neglect the force $\propto V_{ac}^2 (1 + \cos(2\Omega t))$ throughout our analysis.

A 632.8 nm HeNe continuous wave laser with a power of ~ 0.5 mW is focused onto a ~ 1.2 μm -diameter spot and is used both for optomechanical and Raman measurements. Unless otherwise stated, (e.g., inset in Fig.1b and Fig. 4), measurements are performed at the centre of the drum. The beam reflected from the Si/SiO₂/vacuum/graphene layered system is detected using an avalanche photodiode. In the driven regime, the mechanical amplitude at $\Omega/2\pi$ is readout using a lock-in amplifier (Zurich Instruments HFLI). Mechanical mode mapping is implemented using a piezo scanner (E725, PI) and a phase-locked loop. For amplitude calibration, the thermal noise spectrum is derived from the noise power spectral density of the laser beam reflected by the sample, recorded using a spectrum analyzer (FSL3, Rohde & Schwarz). Importantly, displacement calibration is performed assuming that the effective mass of our circular drums is $\tilde{m} = 0.27 m_0$ (Ref. 45), with m_0 the pristine mass of the graphene drum. As discussed in details in Supplementary Section 5, this assumption is validated by two other displacement calibration methods performed on a same drum. These calibrations are completely independent of \tilde{m} . We therefore conclude that to experimental accuracy, our graphene drums are pristine and do not show measurable fingerprints of contamination by molecular adsorbates⁶¹, as expected for a resist-free fabrication process.

Micro-Raman spectroscopy – The Raman scattered light is filtered using a combination of a dichroic mirror and a notch filter. Raman spectra are recorded using a 500 mm monochromator equipped with 300 and 900 grooves/mm gratings, coupled to a cooled CCD array (Princeton Instruments). Let us note that since the lifetime of optical phonons in graphene (~ 1 ps)⁶² is more than three orders of magnitude shorter than the mechanical oscillation period, Raman scattering processes provide an instantaneous measurement of ε_d . However, since our Raman measurements are performed under continuous wave laser illumination, we are dealing with time-averaged dynamical shifts and broadenings of the G-

mode and 2D-mode features. Raman G- and 2D-mode spectra are fit using one Lorentzian and two modified Lorentzian functions, as in Ref. 31 and 63, respectively (Supplementary Section 1). Grüneisen parameters of 1.8 and 2.4 are used to estimate dynamical biaxial strain both in the static and dynamical regime^{31,32}.

Acknowledgements

We thank T. Chen, A. Gloppe and G. Weick for fruitful discussions. We thank the StNano clean room staff

(R. Bernard and S. Siegwald), M. Romeo, F. Chevrier, A. Boulard and the IPCMS workshop for technical support. We acknowledge financial support from the Agence Nationale de Recherche (ANR) under grants H2DH ANR-15-CE24-0016, 2D-POEM ANR-18-ERC1-0009, as well as the Labex NIE project ANR-11-LABX-0058-NIE and USIAS GOLEM project, within the Investissement d'Avenir program ANR-10-IDEX-0002-02.

Competing interests

The authors declare no competing interests.

- * zhxsemi@gmail.com
 † stephane.berciaud@ipcms.unistra.fr
- 1 J. S. Bunch, A. M. van der Zande, S. S. Verbridge, I. W. Frank, D. M. Tanenbaum, J. M. Parpia, H. G. Craighead, and P. L. McEuen, *Science* **315**, 490 (2007).
 - 2 A. Castellanos-Gomez, V. Singh, H. S. J. van der Zant, and G. A. Steele, *Annalen der Physik* **527**, 27 (2015).
 - 3 A. K. Geim and I. V. Grigorieva, *Nature* **499**, 419 (2013).
 - 4 C. Chen, S. Rosenblatt, K. I. Bolotin, W. Kalb, P. Kim, I. Kymissis, H. L. Stormer, T. F. Heinz, and J. Hone, *Nat. Nanotechnol.* **4**, 861 (2009).
 - 5 P. Weber, J. Güttinger, I. Tsioutsios, D. E. Chang, and A. Bachtold, *Nano Lett.* **14**, 2854 (2014).
 - 6 D. Davidovikj, J. J. Slim, S. J. Cartamil-Bueno, H. S. J. Van Der Zant, P. G. Steeneken, and W. J. Venstra, *Nano Lett.* **16**, 2768 (2016).
 - 7 D. Davidovikj, F. Alijani, S. J. Cartamil-Bueno, H. S. J. van der Zant, M. Amabili, and P. G. Steeneken, *Nat. Commun.* **8**, 1253 (2017).
 - 8 J. Lee, Z. Wang, K. He, R. Yang, J. Shan, and P. X.-L. Feng, *Science Advances* **4**, eaao6653 (2018).
 - 9 P. Weber, J. Güttinger, A. Noury, J. Vergara-Cruz, and A. Bachtold, *Nat. Commun.* **7**, 12496 (2016).
 - 10 R. A. Barton, I. R. Storch, V. P. Adiga, R. Sakakibara, B. R. Cipriany, B. Ilic, S. P. Wang, P. Ong, P. L. McEuen, J. M. Parpia, and H. G. Craighead, *Nano Lett.* **12**, 4681 (2012).
 - 11 N. Morell, S. Tepsic, A. Reserbat-Plantey, A. Cepellotti, M. Manca, I. Epstein, A. Isacsson, X. Marie, F. Mauri, and A. Bachtold, *Nano Lett.* **19**, 3143 (2019).
 - 12 R. De Alba, F. Massel, I. R. Storch, T. S. Abhilash, A. Hui, P. L. McEuen, H. G. Craighead, and J. M. Parpia, *Nat. Nanotechnol.* **11**, 741 (2016).
 - 13 J. P. Mathew, R. N. Patel, A. Borah, R. Vijay, and M. M. Deshmukh, *Nat. Nanotechnol.* **11**, 747 (2016).
 - 14 J. Güttinger, A. Noury, P. Weber, A. M. Eriksson, C. Lagoin, J. Moser, C. Eichler, A. Wallraff, A. Isacsson, and A. Bachtold, *Nat. Nanotechnol.* **12**, 631 (2017).
 - 15 V. Singh, S. J. Bosman, B. H. Schneider, Y. M. Blanter, A. Castellanos-Gomez, and G. A. Steele, *Nat. Nanotechnol.* **9**, 820 (2014).
 - 16 X. Song, M. Oksanen, J. Li, P. J. Hakonen, and M. A. Sillanpää, *Phys. Rev. Lett.* **113**, 027404 (2014).
 - 17 A. Castellanos-Gomez, R. van Leeuwen, M. Buscema, H. S. J. van der Zant, G. A. Steele, and W. J. Venstra, *Advanced Materials* **25**, 6719 (2013).
 - 18 N. Morell, A. Reserbat-Plantey, I. Tsioutsios, K. G. Schädler, F. Dubin, F. H. L. Koppens, and A. Bachtold, *Nano Lett.* **16**, 5102 (2016).
 - 19 M. Will, M. Hamer, M. Mller, A. Noury, P. Weber, A. Bachtold, R. V. Gorbachev, C. Stampfer, and J. Gttinger, *Nano Lett.* **17**, 5950 (2017).
 - 20 F. Ye, J. Lee, and P. X. Feng, *Nanoscale* **9** (2017), 10.1039/C7NR04940D.
 - 21 S. Kim, J. Yu, and A. M. van der Zande, *Nano Lett.* **18**, 6686 (2018), <https://doi.org/10.1021/acs.nanolett.8b01926>.
 - 22 S. P. Koenig, N. G. Boddeti, M. L. Dunn, and J. S. Bunch, *Nat. Nanotechnol.* **6**, 543 (2011).
 - 23 D. Lloyd, X. Liu, N. Boddeti, L. Cantley, R. Long, M. L. Dunn, and J. S. Bunch, *Nano Lett.* **17**, 5329 (2017).
 - 24 Z. Dai, L. Liu, and Z. Zhang, *Advanced Materials* **31**, 1970322 (2019).
 - 25 O. Arcizet, V. Jacques, A. Siria, P. Poncharal, P. Vincent, and S. Seidelin, *Nature Phys.* **7**, 879 (2011).
 - 26 J. Teissier, A. Barfuss, P. Appel, E. Neu, and P. Maletinsky, *Phys. Rev. Lett.* **113**, 020503 (2014).
 - 27 P. Ouartchaiyapong, K. W. Lee, B. A. Myers, and A. C. B. Jayich, *Nat. Commun.* **5**, 4429 (2014).
 - 28 I. Yeo, P.-L. de Assis, a. Gloppe, E. Dupont-Ferrier, P. Verlot, N. S. Malik, E. Dupuy, J. Claudon, J.-M. Gérard, a. Auffèves, G. Nogues, S. Seidelin, J.-p. Poizat, O. Arcizet, and M. Richard, *Nat. Nanotechnol.* **9**, 106 (2014).
 - 29 A. Ferrari and D. Basko, *Nat. Nanotechnol.* **8**, 235 (2013).
 - 30 T. M. G. Mohiuddin, A. Lombardo, R. R. Nair, A. Bonetti, G. Savini, R. Jalil, N. Bonini, D. M. Basko, C. Galiotis, N. Marzari, K. S. Novoselov, A. K. Geim, and A. C. Ferrari, *Phys. Rev. B* **79**, 1 (2009).
 - 31 D. Metten, F. Federspiel, M. Romeo, and S. Berciaud, *Phys. Rev. Applied* **2**, 054008 (2014).
 - 32 C. Androulidakis, E. N. Koukaras, J. Parthenios, G. Kalosakas, K. Papagelis, and C. Galiotis, *Scientific Reports* **5**, 18219.
 - 33 X. Zhang, X.-F. Qiao, W. Shi, J.-B. Wu, D.-S. Jiang, and P.-H. Tan, *Chem. Soc. Rev.* **44**, 2757 (2015).
 - 34 J. W. Pomeroy, P. Gkotsis, M. Zhu, G. Leighton, P. Kirby, and M. Kuball, *Journal of Microelectromechanical Systems* **17**, 1315 (2008).
 - 35 C. Xue, L. Zheng, W. Zhang, B. Zhang, and A. Jian, *Journal of Raman Spectroscopy* **38**, 467 (2007).
 - 36 A. Reserbat-Plantey, L. Marty, O. Arcizet, N. Bendiab, and V. Bouchiat, *Nat. Nanotechnol.* **7**, 151 (2012).
 - 37 L. Midolo, A. Schliesser, and A. Fiore, *Nat. Nanotechnol.* **13**, 11 (2018).

- ³⁸ S. Pisana, M. Lazzeri, C. Casiraghi, K. S. Novoselov, A. K. Geim, A. C. Ferrari, and F. Mauri, *Nat. Mater.* **6**, 198 (2007).
- ³⁹ J. E. Lee, G. Ahn, J. Shim, Y. S. Lee, and S. Ryu, *Nat. Commun.* **3**, 1024 (2012).
- ⁴⁰ G. Froehlicher and S. Berciaud, *Phys. Rev. B* **91**, 1 (2015).
- ⁴¹ D. Metten, G. Froehlicher, and S. Berciaud, *2D Mater.* **4**, 014004 (2016).
- ⁴² V. Singh, S. Sengupta, H. S. Solanki, R. Dhall, A. Allain, S. Dhara, P. Pant, and M. M. Deshmukh, *Nanotechnology* **21**, 165204 (2010).
- ⁴³ C. Lee, X. Wei, J. W. Kysar, and J. Hone, *Science* **321**, 385 (2008).
- ⁴⁴ A. H. Nayfeh and D. T. Mook, *Nonlinear Oscillations* (Wiley, 2007).
- ⁴⁵ B. D. Hauer, C. Doolin, K. S. Beach, and J. P. Davis, *Annals of Physics* **339**, 181 (2013).
- ⁴⁶ A. Eichler, J. Moser, M. I. Dykman, and A. Bachtold, *Nat. Commun.* **4**, 2843 (2013).
- ⁴⁷ R. Fandan, J. Pedrs, A. Hernandez-Mnguez, F. Iikawa, P. V. Santos, A. Bosc, and F. Calle, *Nano Letters* **20**, 402 (2020).
- ⁴⁸ J.-U. Lee, D. Yoon, and H. Cheong, *Nano Lett.* **12**, 4444 (2012).
- ⁴⁹ F. Yang, F. Rochau, J. S. Huber, A. Brioussel, G. Rastelli, E. M. Weig, and E. Scheer, *Phys. Rev. Lett.* **122**, 154301 (2019).
- ⁵⁰ J. Atalaya, A. Isacson, and J. M. Kinaret, *Nano Lett.* **8**, 4196 (2008).
- ⁵¹ M. L. Ackerman, P. Kumar, M. Neek-Amal, P. M. Thibado, F. M. Peeters, and S. Singh, *Phys. Rev. Lett.* **117**, 126801 (2016).
- ⁵² J. W. Kang, H.-W. Kim, K.-S. Kim, and J. H. Lee, *Current Applied Physics* **13**, 789 (2013).
- ⁵³ G. Wang, A. Chernikov, M. M. Glazov, T. F. Heinz, X. Marie, T. Amand, and B. Urbaszek, *Rev. Mod. Phys.* **90**, 021001 (2018).
- ⁵⁴ C. Palacios-Berraquero, D. M. Kara, A. R.-P. Montblanch, M. Barbone, P. Latawiec, D. Yoon, A. K. Ott, M. Loncar, A. C. Ferrari, and M. Atatre, *Nat. Commun.* **8**, 15093 (2017).
- ⁵⁵ A. Branny, S. Kumar, R. Proux, and B. D. Gerardot, *Nat. Commun.* **8**, 15053 (2017).
- ⁵⁶ Y. Zhou, G. Scuri, J. Sung, R. J. Gelly, D. S. Wild, K. De Greve, A. Y. Joe, T. Taniguchi, K. Watanabe, P. Kim, M. D. Lukin, and H. Park, *Phys. Rev. Lett.* **124**, 027401 (2020).
- ⁵⁷ M. Gibertini, M. Koperski, A. F. Morpurgo, and K. S. Novoselov, *Nat. Nanotechnol.* **14**, 408 (2019).
- ⁵⁸ M. Šiškins, M. Lee, S. Mañas-Valero, E. Coronado, Y. M. Blanter, H. S. van der Zant, and P. G. Steeneken, *arXiv preprint arXiv:1911.08537* (2019).
- ⁵⁹ S. Jiang, H. Xie, J. Shan, and K. F. Mak, *arXiv preprint arXiv:2001.03153* (2020).
- ⁶⁰ Y. Huang, X. Wang, X. Zhang, X. Chen, B. Li, B. Wang, M. Huang, C. Zhu, X. Zhang, W. S. Bacsá, F. Ding, and R. S. Ruoff, *Phys. Rev. Lett.* **120**, 186104 (2018).
- ⁶¹ S. Berciaud, S. Ryu, L. E. Brus, and T. F. Heinz, *Nano Lett.* **9**, 346 (2009).
- ⁶² N. Bonini, M. Lazzeri, N. Marzari, and F. Mauri, *Phys. Rev. Lett.* **99**, 176802 (2007).
- ⁶³ S. Berciaud, X. Li, H. Htoon, L. E. Brus, S. K. Doorn, and T. F. Heinz, *Nano Lett.* **13**, 3517 (2013).
- ⁶⁴ J. Maultzsch, S. Reich, and C. Thomsen, *Phys. Rev. B* **70**, 155403 (2004).
- ⁶⁵ D. M. Basko, *Phys. Rev. B* **78**, 125418 (2008).
- ⁶⁶ P. Venezuela, M. Lazzeri, and F. Mauri, *Phys. Rev. B* **84**, 1 (2011).
- ⁶⁷ C.-F. Chen, C.-H. Park, B. W. Boudouris, J. Horng, B. Geng, C. Girit, A. Zettl, M. F. Crommie, R. A. Segalman, S. G. Louie, and F. Wang, *Nature* **471**, 617 (2011).
- ⁶⁸ P. Blake, E. W. Hill, A. H. Castro Neto, K. S. Novoselov, D. Jiang, R. Yang, T. J. Booth, and A. K. Geim, *Applied Physics Letters* **91**, 2007 (2007).
- ⁶⁹ D. Yoon, H. Moon, Y.-W. Son, J. S. Choi, B. H. Park, Y. H. Cha, Y. D. Kim, and H. Cheong, *Phys. Rev. B* **80**, 125422 (2009).
- ⁷⁰ D. Metten, G. Froehlicher, and S. Berciaud, *Phys. Status Solidi B* **252**, 2390 (2015).
- ⁷¹ K. I. Bolotin, K. J. Sikes, Z. Jiang, M. Klima, G. Fudenberg, J. Hone, P. Kim, and H. L. Stormer, *Solid State Commun.* **146**, 351 (2008).
- ⁷² S. Berciaud, M. Potemski, and C. Faugeras, *Nano Lett.* **14**, 4548 (2014).
- ⁷³ C. Schwarz, PhD dissertation, Institut Neel, Grenoble (2016).
- ⁷⁴ I. Calizo, A. A. Balandin, W. Bao, F. Miao, and C. N. Lau, *Nano Lett.* **7**, 2645 (2007).
- ⁷⁵ D. Yoon, Y.-W. Son, and H. Cheong, *Nano Lett.* **11**, 3227 (2011).

Supplementary Information for: Dynamically-enhanced strain in atomically-thin resonators

CONTENTS

References	8
Introduction	11
S1. Raman scattering in graphene	11
S1a. The G mode and the 2D mode	11
S1b. Fitting the Raman 2D-mode spectra	11
S2. Sample design and interference effects	14
S3. Elementary modelling of static and dynamical strain	16
S3a. Static strain	16
S3b. Dynamical strain induced by harmonic vibrations	16
S4. Static displacement and equilibrium position shift	17
S4a. Determination of the static displacement	17
S4b. Equilibrium position shift in the driven regime	19
S5. Displacement calibration	20
S5a. Calibration Methods	20
S5a1. C_1 : Thermal noise	20
S5a2. DC reflectance-based methods	21
S5b. Discussion on the effective mass of graphene drums	21
S6. Mechanical response of driven graphene drums	23
S6a. Linear response	23
S6b. Non-linear mechanical response	24
S7. Effects of laser-induced heating.	26
S8. Supplementary data on device 1	28
S9. Supplementary data on device 2	30
S10. Supplementary data on device 3	34

INTRODUCTION

This supplementary information file is organised as follows. In Section S1, we provide details on the Raman scattering response of graphene and on our fitting procedure. In Section S2 and Sec. S3, we outline the sample design and discuss an elementary mechanical model, respectively, before discussing, in Sec. S4, how optical interference effects allow estimating the static displacement ξ of a graphene drum and the static strain ε_s it undergoes. In Section S5, we present a comprehensive displacement calibration scheme using three different methods that yield a consistent and accurate determination of the root mean square (RMS) displacement z_{rms} in the driven regime. These results also allow us to conclude that, within experimental accuracy, the effective mass of our drum is that of a pristine graphene monolayer. In Section S6, we present a basic modelling of the mechanical response of graphene both in the linear and non-linear regime. Laser-induced heating effects are addressed in Sec. S7. Finally, Sec. S8, S9, S10 provide supplementary data on devices 1, 2 and 3, respectively. These data complement and/or bolster the data shown in the main text. Devices 1, 2 and 3 have very similar designs.

S1. RAMAN SCATTERING IN GRAPHENE

S1a. The G mode and the 2D mode

As introduced in the main text, our study focuses on the well-documented G mode and 2D modes in graphene²⁹. Simplified sketches of the G- and 2D-mode processes are shown in Fig. S1. The G mode is a one phonon non-resonant process originating from in-plane (LO and TO) zero momentum optical phonons, that is at the centre (Γ point) of the Brillouin zone. The G-mode feature is commonly described as a single, quasi-Lorentzian feature⁴⁰. The 2D-mode is a resonant, symmetry allowed two-phonon process involving a pair of near-zone edge TO phonons near the edges of the Brillouin zone (K and K' points)^{64–66}. This 2D-mode frequency depends both on the electronic and phononic dispersion and hence on the incoming laser photon energy. The 2D mode-lineshape is *a priori* very complex⁶⁵. In the case of suspended graphene, this lineshape is phenomenologically fit to the sum of two modified Lorentzian profiles, as in Ref. 63.

S1b. Fitting the Raman 2D-mode spectra

As discussed above and in Ref. 63, the 2D-mode lineshape in suspended graphene is asymmetric and best fit with the sum of two modified Lorentzian profiles, as exemplified in Fig. S2 and in Fig. 2b and 3b. The 2D-mode frequency ω_{2D} discussed in the main manuscript refers to the more intense $2D^-$ sub-feature unless otherwise specified (Fig. S3), while the 2D-mode intensity I_{2D} refers to the *total* integrated intensity of both $2D^-$ and $2D^+$ sub-features. As we show in Fig. S3, both low- and high-frequency 2D-mode sub-features are similarly affected in the driven regime.

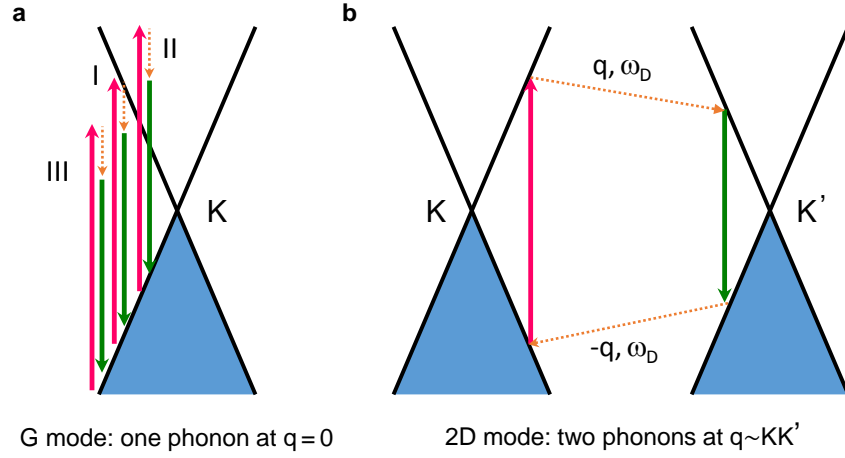


FIG. S1. **Raman scattering processes in graphene.** The pink, green and dashed orange arrows in **a** and **b** indicate incoming photons, scattered photons and scattered phonons, respectively. The G mode (**a**) is a one-phonon process involving zone-center optical phonons (LO and TO)²⁹. Although resonant processes (I) may contribute to the G-mode intensity, the G-mode feature arises for the most part from the quantum interference between non-resonant processes (II, III) across the whole Brillouin zone⁶⁷. The 2D mode (**b**) is a resonant inter-valley process involving a pair of near zone-edge TO phonons with opposite momenta $\pm q$. Here, for clarity, we only represent the so-called inner process involving phonons with momenta smaller than KK' (Ref. 63 and 66).

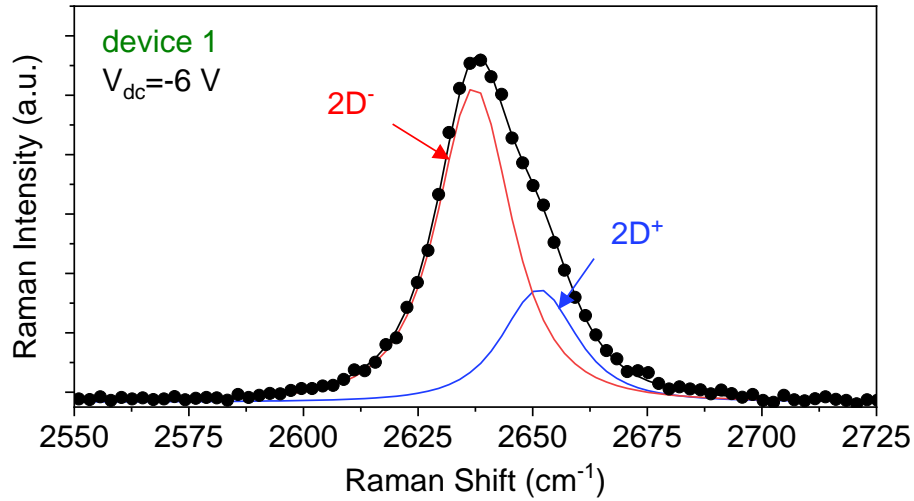


FIG. S2. **Fitting the Raman 2D-mode spectra in a suspended graphene drum.** Modified Lorentzian fit of the 2D-mode feature in suspended graphene using two sub-features, denoted $2D^-$ and $2D^+$, as in Ref. 63.

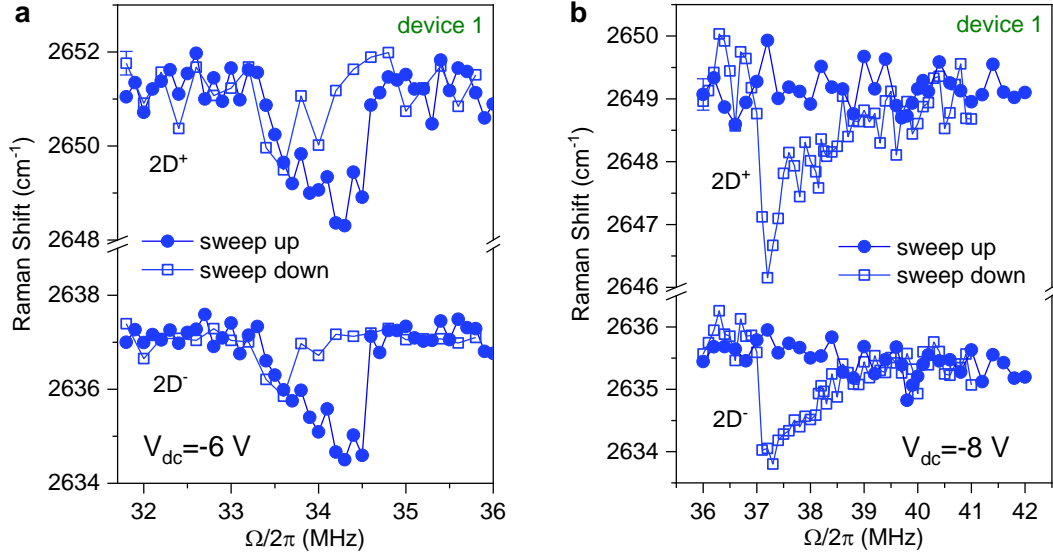


FIG. S3. **Fitting the Raman 2D-mode spectra in a resonantly-driven graphene drum.** Frequency of the two 2D mode subfeatures (ω_{2D^+} and ω_{2D^-}) as a function of the drive frequency $\Omega/2\pi$ for both upward (circles) and downward (squares) drive frequency sweeps at $V_{dc} = -8$ V (a) and $V_{dc} = -6$ V (b) in device 1 (see also Fig. S13 and Fig. 3, respectively). Only one error bar is included in each plot for clarity.

S2. SAMPLE DESIGN AND INTERFERENCE EFFECTS

Figure S4a shows the vacuum/graphene/vacuum/SiO₂/Si multilayered system discussed in the main text. Due to optical interference effects, the reflectance and Raman scattering intensity depend on the laser wavelength, hole depth (d_{vac}) and residual SiO₂ thickness (d_{SiO_2}). Starting from a given sample geometry, we have used well-established models to compute the interference enhancement factors allowing to quantitatively predict the dependence of the sample reflectance^{7,68} and Raman scattered intensity^{31,41,69} as a function of the deflection of the graphene layer, denoted ξ . As we shall see in Sec. S4 and Sec. S5, this modelling will allow us to accurately determine ξ in graphene drums and to calibrate displacements in the driven regime.

We have optimized the sample geometry to provide both large transduction coefficient for displacement readout (see Methods) and sufficiently intense Raman scattering signal. First, 285nm-SiO₂/Si (*p*-doped) substrates are chosen to easily locate monolayer graphene flakes by optical microscopy⁶⁸. With $d_{\text{vac}} = 250 \pm 5$ nm (correspondingly, $d_{\text{SiO}_2} = 35$ nm), the optical reflectance varies quasi-linearly with the static deflection of the membrane ξ over the range $\xi = 30$ -100 nm, ensuring a constant transduction coefficient for optical readout of the root mean square (RMS) mechanical displacement around an equilibrium position (Fig. S4b). At the same time, optical interferences lead to large enough Raman intensities, as shown in the calculated Raman enhancement factors^{31,41,69} in Fig. S4c,d. Third, the hole diameters $2a = 5$ μm and 6 μm , are chosen such that the resonance frequency of the fundamental flexural mode (Sec. S6) lies within the 50 MHz bandwidth of our detection setup.

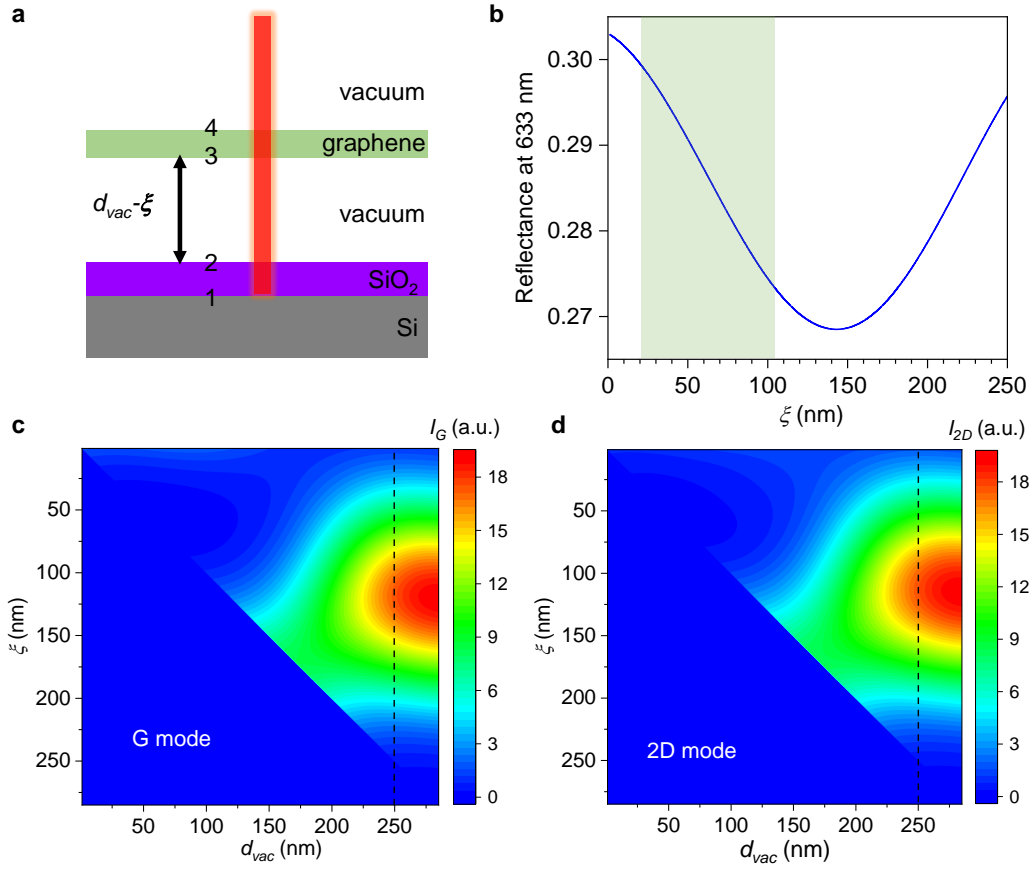


FIG. S4. **Sample geometry and interference effects.** **a**, Multilayer model for our devices, where the labels 1 – 4 represent the interfaces in the system. $d_{vac} - \xi$ is the gap between suspended graphene, displaced by ξ using a DC gate bias, and the SiO₂ surface. **b**, Calculated reflectance as a function of ξ in the case of a monolayer graphene for $d_{vac} = 250$ nm and a laser wavelength of 632.8 nm. The light-green area denotes the linear region, where a large and constant transduction coefficient allows interferometric readout of the mechanical vibrations. At a small ξ , the reflectance is close to a maximum, resulting in a sharp decrease of the transduction coefficient. **c, d**, Contour plots of the G- and 2D-mode intensity enhancement factors (Sec. S4) as a function of d_{vac} and ξ under optical excitation at 632.8 nm. The SiO₂ thickness is 285 nm. The black dashed lines highlight the results at $d_{vac} = 250$ nm.

S3. ELEMENTARY MODELLING OF STATIC AND DYNAMICAL STRAIN

S3a. Static strain

For simplicity, we assume that under an electrostatic pressure (here, a finite gate bias V_{dc}), our circular graphene drums (radius r) adopt a parabolic profile^{22,41}. The downward deflection $\xi(r)$ thus writes:

$$\xi(r) = \xi(0) \left(1 - \frac{r^2}{a^2}\right) \quad (\text{S1})$$

r is the radial coordinate $\xi(0)$ is the static deflection of the membrane's center ($r = 0$).

The elongation ΔL is:

$$\Delta L = \int_{-a}^a \sqrt{1 + [\xi'(r)]^2} dr - 2a \quad (\text{S2})$$

For small deflections, *i.e.*, $\xi(r) \ll a$, the static strain ε_s writes:

$$\varepsilon_s = \frac{\Delta L}{2a} = \frac{2}{3} \left(\frac{\xi}{a}\right)^2. \quad (\text{S3})$$

In Eq. (S3) and in the following, $\xi(0)$ will be denoted ξ for simplicity.

Besides, under biaxial strain, the Raman frequency shift ($\Delta\omega_i$, with $i = \text{G}, 2\text{D}$) relative to the unperturbed values $\omega_{i,0}$ are linked to ε_s by^{31,32}:

$$\Delta\omega_i = 2\gamma_i \varepsilon_s \omega_{i,0} \quad (\text{S4})$$

with the Grüneisen parameters $\gamma_{\text{G}} = 1.8$ and $\gamma_{2\text{D}} = 2.4$, as measured in similar circular graphene drums^{31,32}. Eq. (S3) and (S4) are combined to estimate ξ . Fig. S6 shows ε_s and $\Delta\omega_{2\text{D}}$ as a function of ξ for $a = 3 \mu\text{m}$. By comparing to the experimental data recorded on device 1 (Fig. S5 and Fig. 1d in the main text), we estimate $\xi \approx 42 \text{ nm}$ and $\xi \approx 63 \text{ nm}$ for $V_{\text{dc}} = -6 \text{ V}$ and $V_{\text{dc}} = -8 \text{ V}$, respectively.

Starting from the estimated ξ based on the V_{dc} -dependent Raman mode frequencies, we can further cross-check our calibration by another method based on the dependence of Raman intensities ($I_{\text{G}}, I_{2\text{D}}$) on ξ (Sec. S4 and Fig. S4c,d and S7). The very good match between experimentally measured $I_{\text{G}}, I_{2\text{D}}$, their ratio ($I_{2\text{D}}/I_{\text{G}}$) and calculations based on an optical interference model^{31,41,69} allows us to further validate our calibration of ξ .

S3b. Dynamical strain induced by harmonic vibrations

Here we compare our measurements of dynamically-induced strain ε_{d} obtained under strong non-linear driving to the expected values under a harmonic oscillation with the same RMS (root mean square) amplitude. We assume that under the application of a sinusoidal driving force at frequency $\Omega/2\pi$, the drum maintains a parabolic shape and that $\xi(t) = \xi + \sqrt{2} z_{\text{rms}} \cos(\Omega t + \varphi)$, with z the mechanical amplitude and φ the phase difference between the drive and the mechanical response (Sec. S6). The *harmonic* dynamical strain $\varepsilon_{\text{d}}^{\text{h}}$ can be estimated by inserting $\xi(t)$ into Eq.(S3) and averaging over one oscillation period:

$$\varepsilon_{\text{d}}^{\text{h}} = \frac{2}{3} \left(\frac{z_{\text{rms}}}{a}\right)^2 \quad (\text{S5})$$

Eq. (S5) is then used with the measured RMS displacements z_{rms} to compare $\varepsilon_{\text{d}}^{\text{h}}$ with the measured ε_{d} in Fig. 2-4 in the main manuscript.

S4. STATIC DISPLACEMENT AND EQUILIBRIUM POSITION SHIFT

S4a. Determination of the static displacement

Using an multiple reflection model as in Ref. 31, 41, and 69, the intensity enhancement factors of the G- and 2D-mode features can be calculated as a function of ξ for $d_{\text{SiO}_2} = 35$ nm, $d_{\text{vac}} = 250$ nm, and a laser wavelength of 632.8 nm (Fig. S4c,d). Both I_G and I_{2D} monotonically increase with ξ for $\xi \lesssim 125$ nm, above which they monotonically decrease after reaching an intensity maximum. In particular, $I_G(\xi)$ and $I_{2D}(\xi)$ can be approximated as linear in the range $\xi = 20 - 70$ nm (Fig. S7), which corresponds to the static displacements explored in our study. The data points in Fig. S7a represent the equilibrium deflection (ξ) obtained at various V_{dc} and extracted from the measured Raman G- and 2D-mode frequencies (Sec. S3 and Fig. S5-S6). We can see that using an appropriate scaling factor that essentially accounts for the Raman susceptibilities of the G- and 2D-modes in the “interference-free” case^{41,70}, the intensity ratio I_{2D}/I_G matches very well with theoretical predictions (Fig. S7b). This agreement validates our strain-based estimation of ξ and provides a solid ground to calibrate the RMS displacements (Sec. S5).

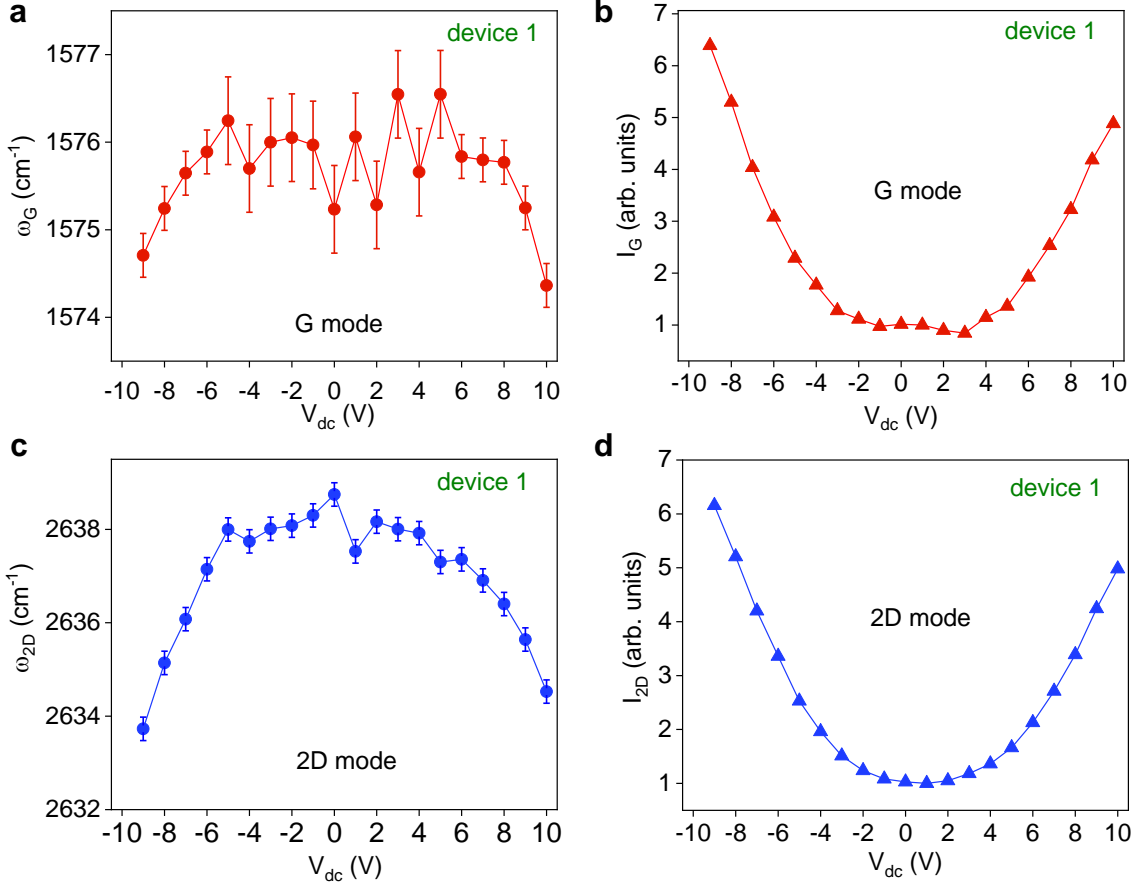


FIG. S5. **Probing static strain in an electrostatically gated graphene drum.** Frequency of the G- (a) and 2D-mode (c) features as a function of V_{dc} in device 1 (see also Fig. 1d in the main manuscript for selected raw spectra). Integrated intensity of the (c) G-mode (I_G) and (d) 2D-mode (I_{2D}) features as a function of V_{dc} . The integrated intensities are normalized with respect to the values measured at $V_{\text{dc}} = 1$ V.

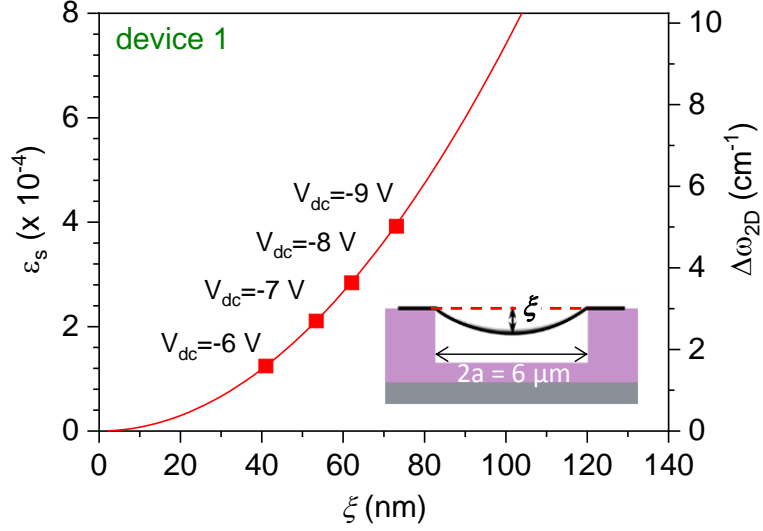


FIG. S6. **Determination of the static tensile strain and static deflection.** Calculated static strain ε_s using Eq. (S3) and corresponding frequency softening (Sec. S3) of the 2D mode $\Delta\omega_{2D}$ as a function of ξ for a hole diameter $2a = 6 \mu\text{m}$. The red symbols show $\Delta\omega_{2D}$ (from Fig. S5c) and the estimated ξ for V_{dc} ranging from -5 V to -8 V. The device geometry is recalled as an inset.

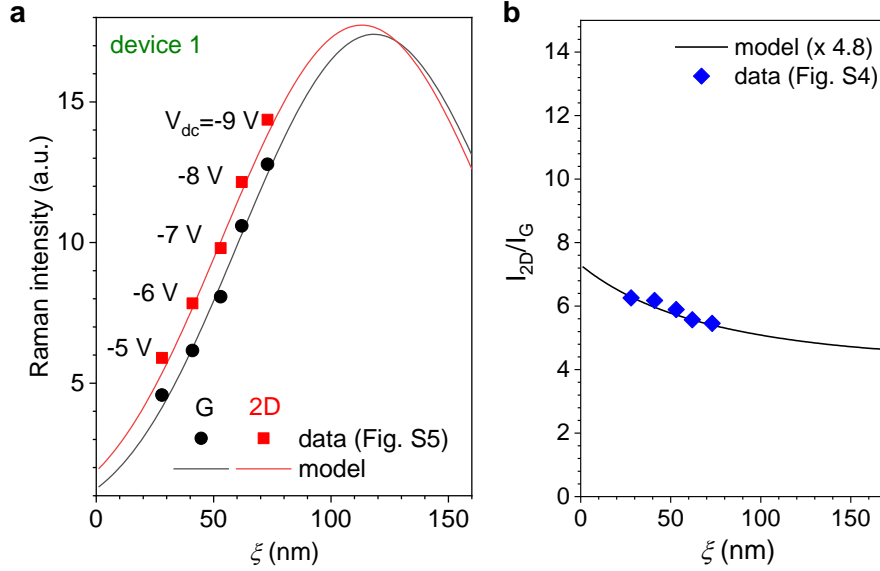


FIG. S7. **Raman scattering intensity as a function of the static deflection.** **a**, Calculated Raman intensity enhancement factors (solid lines) and measured Raman intensities (symbols) for the G (black) and 2D (red) modes as a function of ξ . The G- and 2D-mode intensities are extracted from Fig. S5b and d, respectively and scaled by a constant factor to allow comparison with the Raman intensity enhancement factors (Fig. S4c,d). The values of ξ associated with the experimental data are deduced from the strain-induced 2D-mode softening (Sec. S4a and Fig. S6). **b**, Measured Raman intensity ratio (I_{2D}/I_G) as a function of ξ (blue symbols). The solid line is the ratio of the Raman intensity enhancement factors multiplied by a scaling factor of 4.8 that corresponds to the “interference-free case”⁷⁰.

S4b. Equilibrium position shift in the driven regime

In the linear regime, a graphene drum vibrates harmonically in a symmetric potential $U(\xi)$ (inset in Fig. 2e in the main text) with respect to the static equilibrium displacement ξ_{eq} (Fig. 2e). Under non-linear driving, the displacements are large enough such that the drum explores an asymmetric potential^{44,46}. The drum now vibrates symmetrically with respect to an equilibrium position shifted by $\Delta\xi_{\text{eq}}$, for which the Raman intensity enhancement factor (Fig. S4, S5, S7) is different. As a result, the measured Raman intensities become dependent on the driving force as the graphene drum is driven non-linearly, as evidenced in Fig. 2e and 3a, where Raman intensity drops by $\sim 20\%$ (at $V_{\text{dc}} = -8$ V) and $\sim 10\%$ (at $V_{\text{dc}} = -6$ V) are consistently observed. As discussed in the main text, these intensity drops correspond to an upshift of the equilibrium position (Fig. S7). Similar equilibrium position upshifts are discussed in device 3 (Fig. 4).

S5. DISPLACEMENT CALIBRATION

S5a. Calibration Methods

A careful displacement calibration is essential to make sure that our assumption of a constant optomechanical transduction coefficient remains valid at the largest displacements attained in the non-linear regime. In addition, displacement calibration permits an estimation of the effective mass (see below) and allow demonstrating the pristine character of our samples and the generality of our findings.

The RMS displacements z_{rms} of our monolayer graphene drums are calibrated using three distinct methods described in the following subsections. The transduction coefficients β_i (nm/mV) (with $i = 1, 2, 3$) that connect the RMS voltage measured with our lock-in amplifier to z_{rms} are found to be very similar for the 3 methods and are summarized in Table S1 for device 2 at $V_{\text{dc}} = -8$ V.

Calibration method	β_i (nm/mV), $i = 1, 2, 3$
C_1 : Thermal noise	1.1 ± 0.15
C_2 : DC reflectance and Raman spectroscopy	1.0 ± 0.10
C_3 : DC reflectance and interference model	1.2 ± 0.20

TABLE S1. Displacement calibration methods. Transduction coefficient β_i (nm/mV), $i = 1, 2, 3$ connecting the measured RMS voltage on our lock-in amplifier to the measured RMS displacement z_{rms} of a driven graphene drum for three calibration methods (C_i , $i = 1, 2, 3$). Measurements were performed on device 2 at $V_{\text{dc}} = -8$ V.

S5a1. C_1 : Thermal noise

The mechanical oscillations of the graphene drum its thermal noise power spectral density (PSD) are related via⁴⁵:

$$\langle z_n^2(t) \rangle = \int_0^\infty df S_{zz}(f) \quad (\text{S6})$$

where $f = \Omega/2\pi$ is the mechanical frequency, $\langle z_n^2(t) \rangle$ is the mean-square amplitude of vibration of the n -th mode, which one-sided displacement spectral density $S_{zz}(f)$ writes:

$$S_{zz}(f) = \frac{k_B T f_n}{2\pi^3 \tilde{m}_n Q_n [(f^2 - f_n^2)^2 + (f f_n / Q_n)^2]} \quad (\text{S7})$$

where k_B , T , f_n , Q_n and \tilde{m}_n are the Boltzmann constant, the temperature (here taken equal to the ambient temperature), the resonance frequency, the quality factor and the effective mass of the n -th mode, respectively. Importantly, the surface mass density of our drum is assumed to be equal to that of pristine monolayer graphene (see Sec. S5b for a discussion on the relevance of this assumption). In the following, we will focus on the fundamental mechanical mode discussed in the main text.

The thermal noise PSD $S_{zz}(f)$ of the graphene drum is determined from the spectrum $V(f)$ of the output voltage of our avalanche photodiode, measured using a spectrum analyser. The resulting PSD is $S_{VV}(f) = V(f)^2/\Delta f$, where Δf is the resolution bandwidth (typically in the $10^2 - 10^3$ Hz range). The measured signal includes a flat noise floor (S_{VV}^w) due to the dark current noise of the photodiode and other sources of white noise and is connected to $S_{zz}(f)$ through:

$$S_{VV}(f) = S_{VV}^w + \eta S_{zz}(f), \quad (\text{S8})$$

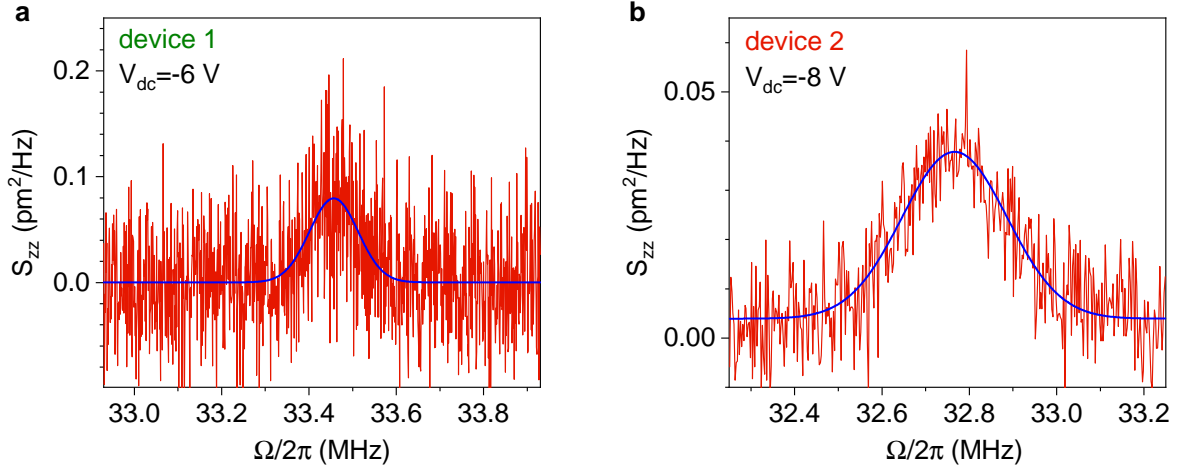


FIG. S8. Displacement calibration method C_1 . Thermal noise power spectral density (PSD) of the fundamental mode of device 1 at $V_{dc} = -6$ V (a) and device 2 at $V_{dc} = -8$ V (b). The blue curves are the fit of the PSD using Eq. (S7).

where η is another transduction coefficient expressed in V^2/m^2 . η is obtained by fitting the measured $S_{VV}(f)$ by Eq. (S8), as in Fig. S8. Finally, to calibrate the mechanical amplitude of the driven graphene drum measured using our lock-in amplifier, we simultaneously record the mechanical amplitude in the linear regime (typically with $V_{ac} = 1$ mV) using the spectrum analyser and our lock-in amplifier and deduce β_1 (Table S1). This calibration method was applied to all the devices studied in this work at various V_{dc} .

S5a2. DC reflectance-based methods

The following two methods rely on a measurement of the DC reflectance of the sample (proportional to the intensity of the 632.8 nm laser beam reflected by the sample, see Fig. S4) as a function of V_{dc} , combined with a calibration of the gate-dependent static deflection ξ (Fig. S4 and Fig. S6). Both methods connect the DC reflectance to ξ and yield the transduction coefficients β_2 and β_3 .

C₂: DC reflectance and Raman spectroscopy. With calibration C_2 , ξ is estimated through the gate-dependent spectral shifts of the Raman G and 2D modes as discussed in Sec. S3, Sec. S4 and Fig. S5-S6). Coincidentally, the gate-induced changes of the DC reflectance are monitored with our lock-in amplifier.

C₃: DC reflectance and interference model. As discussed in Sec. S2 and Fig. S4, an interference calculation^{68,69} can be applied to obtain the reflectance of our samples as a function of ξ . Fig. S9 shows the calculated reflectance together with our measurements of the reflected laser intensity vs V_{dc} , scaled to match the simulated values.

S5b. Discussion on the effective mass of graphene drums

The calibration of the displacement of a nanomechanical system with thermal noise measurements (C_1) requires accurate knowledge of its effective mass. Here, in Sec. S5a1, we have considered the surface mass density of pristine monolayer graphene ($\approx 7.5 \times 10^{-7}$ kg/m²). For the fundamental mechanical mode of circular drum, the rest mass of graphene has to be scaled by a factor ≈ 0.27 (Ref. 45), such that the *effective* mass of our 6 μm -diameter drum is

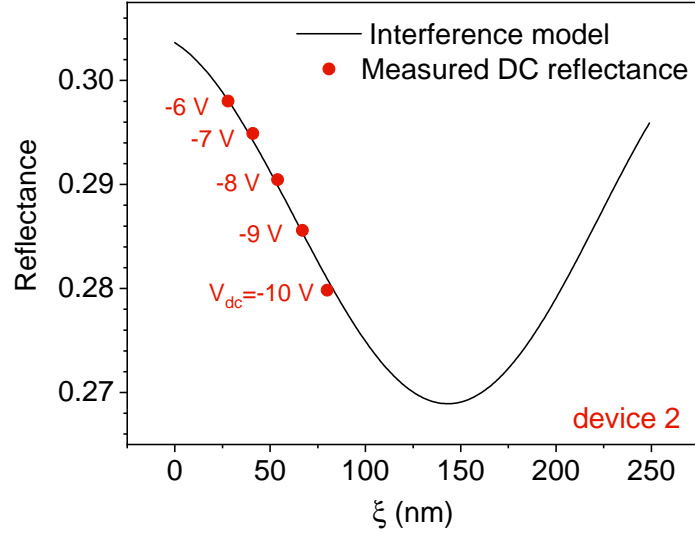


FIG. S9. **Displacement calibration method C_3** . Calculated (solid line) and measured (symbols) sample reflectance at 632.8 nm as a function of the static displacement ξ .

$\tilde{m}_0 \approx 5.7 \times 10^{-18}$ kg. Calibration C_2 and C_3 are totally independent of \tilde{m} and yield transduction coefficients $\beta_{1,2}$ that are, within experimental accuracy, equal the coefficient β_1 obtained using thermal noise measurements considering \tilde{m}_0 (see values and associated errorbars in Table S1). This key result justifies our assumption that $\tilde{m} = \tilde{m}_0$.

Following previous reports, we could have expected that \tilde{m} would *a priori* exceed \tilde{m}_0 due to the presence of molecular adsorbates and other sources of contamination⁵. Here, our devices are made from freshly exfoliated natural graphite flakes using a dry, resist-free transfer method and then held in high vacuum. Such freely suspended graphene membranes have consistently shown intrinsic electronic⁷¹ and optical^{61,63,72} properties and our study also demonstrates that the same holds for their mechanical figures of merit.

Let us note in closing that assuming $\tilde{m} > \tilde{m}_0$ when using method C_1 would lead to smaller calibrated displacements than those estimated assuming \tilde{m}_0 . Smaller displacements would lead to smaller values of ε_d^h calculated through Eq. (S5) and to a larger discrepancy between ε_d^h and the enhanced ε_d determined from our Raman measurements in resonantly driven graphene drums.

S6. MECHANICAL RESPONSE OF DRIVEN GRAPHENE DRUMS

The displacement of our graphene drums can be modeled as that of a driven non-linear oscillator by⁴⁴:

$$\ddot{z} + \frac{\Omega_0}{Q}\dot{z} + \Omega_0^2 z + \alpha_2 z^2 + \alpha_3 z^3 = \frac{\tilde{F}_{el}}{\tilde{m}} \cos(\Omega t) \quad (\text{S9})$$

where z is the mechanical displacement at the membrane center, $\Omega_0/2\pi$ is the resonance frequency in the linear regime, Q is the quality factor and Ω_0/Q is the linear damping rate, α_2 , α_3 are the quadratic and the cubic spring constant, respectively. Finally, $\tilde{m} = 0.27 m_0$ (with m_0 the rest mass of the graphene drum) is the effective mass with a correction factor that accounts for the mode shape of the fundamental resonance of a clamped circular membrane^{5-7,45} and \tilde{F}_{el} is the effective applied electrostatic force.

S6a. Linear response

In the linear response regime, $\alpha_{2,3} = 0$, Eq. (S9) is the well-known differential equation of a driven harmonic oscillator. Assuming a harmonic solution $z(t) = z_0 e^{i\Omega t}$, one gets:

$$z_0 = \frac{\tilde{F}_{el}/\tilde{m}}{\Omega_0^2 - \Omega^2 + i\Omega_0\Omega/Q}. \quad (\text{S10})$$

For the fundamental mechanical mode of a thin circular membrane resonator under a sufficiently high built-in tension T_0 (as is the case for our graphene drums) Ω_0 writes⁷³

$$\Omega_0 = 2\pi f_0 = u_{01} \sqrt{\frac{T_0}{\sigma a^2}}, \quad (\text{S11})$$

where $\sigma \approx 7.5 \times 10^{-7}$ kg/m² is the surface mass density of pristine graphene and $u_{01} \approx 2.405$ is the first zero of the zero-order Bessel function. Therefore, T_0 writes

$$T_0 = 0.69 \pi^2 f_0^2 \sigma a^2, \quad (\text{S12})$$

where $T_0 = E_{1LG} \varepsilon_s / (1 - \nu^2)$ (Ref. 73), with $E_{1LG} = 340$ Nm⁻¹ and $\nu = 0.16$ the Young modulus and Poisson ratio of pristine monolayer graphene, respectively⁴³. Eq. (S12) is then used to compute the built-in and the gate-induced static strain discussed in the text. These strain values can be compared with estimates from the G- and 2D-mode softenings.

From Eq. (S10), we get

$$|z_0|^2 = \frac{\left(\tilde{F}_{el}/\tilde{m}\right)^2}{(\Omega_0^2 - \Omega^2)^2 + (\Omega\Omega_0/Q)^2}, \quad (\text{S13})$$

Eq. (S13) can be used to fit the frequency-response curve in the linear response region and extract Q , as in Fig. 1. Furthermore, near resonance ($|\Omega - \Omega_0| \ll \Omega_0$) and for $Q \gg 1$, Eq. (S13) simplifies as:

$$|z_0|^2 = \frac{\tilde{F}_{el}^2}{4\tilde{m}^2\Omega_0^2} \frac{1}{(\Omega - \Omega_0)^2 + \Omega_0^2/4Q^2} \quad (\text{S14})$$

which is a Lorentzian lineshape with full width at half maximum Ω_0/Q .

S6b. Non-linear mechanical response

Eq. (S9) can be rewritten by introducing an effective cubic spring constant^{5,44}, $\tilde{\alpha}_3 = \alpha_3 - \frac{10\alpha_2^2}{9\Omega_0^2}$,

$$\ddot{z} + \frac{\Omega_0}{Q}\dot{z} + \Omega_0^2 z + \tilde{\alpha}_3 z^3 = \frac{\tilde{F}_{el}}{\tilde{m}} \cos(\Omega t). \quad (\text{S15})$$

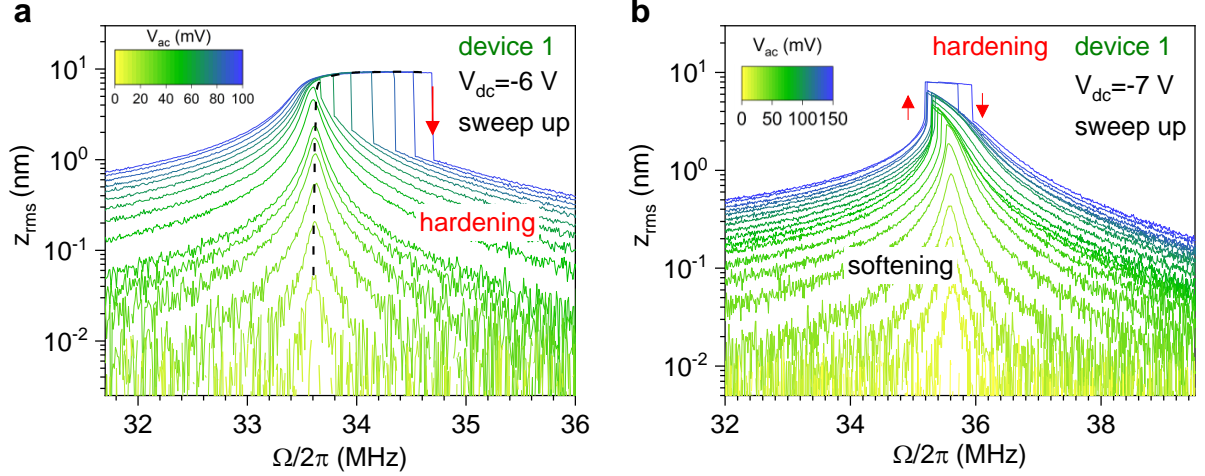


FIG. S10. **Mechanical non-linearities in graphene drums (1)**. Frequency-response curves obtained by sweeping the drive frequency upward at $V_{dc} = -6$ V (a) and $V_{dc} = -7$ V (b) on device 1. At $V_{dc} = -7$ V, a nonlinear softening to hardening transition is revealed above $V_{ac} = 130$ mV.

To obtain the non-linear coefficient in Eq. S15, we can approximate the solution of Eq. S15 by a truncated Fourier series, restricted here to first order. This approach allows to establish the analytical expression of the so-called *backbone curve* that connects the maximum amplitude z_0 to the drive frequency $\tilde{\Omega}_0/2\pi$ at which it is obtained. Following Refs. 7 and 44, we get:

$$\tilde{\Omega}_0 = \Omega_0 + \frac{3}{8} \frac{\tilde{\alpha}_3}{\Omega_0} z_0^2 \quad (\text{S16})$$

As the driving force is increased, the onset of third-order non-linearities leads to resonance frequency hardening for $\tilde{\alpha}_3 > 0$ (see data at $V_{dc} = -6$ V in Fig. 3 and Fig. S11 and at $V_{dc} = -5$ V in Fig. S10 and S11), and to resonance frequency softening for $\tilde{\alpha}_3 < 0$ (see Fig. 2 in the main text, for $V_{dc} = -8$ V), respectively. As expected from Eq. (S16), a parabolic backbone curve is observed at $V_{dc} = -8$ V and to a lesser extent at $V_{dc} = -5$ V (Fig. S11). However, the backbone curve fully saturates at $V_{dc} = -6$ V for $V_{ac} > 40$ mV (Fig. 3a, Fig. 3f and Fig. S11b). In this strongly non-linear regime, significant Fourier components are expected at harmonics of the drive frequency, as experimentally verified on device 2 in Fig. S15, and the first order expansion is insufficient.

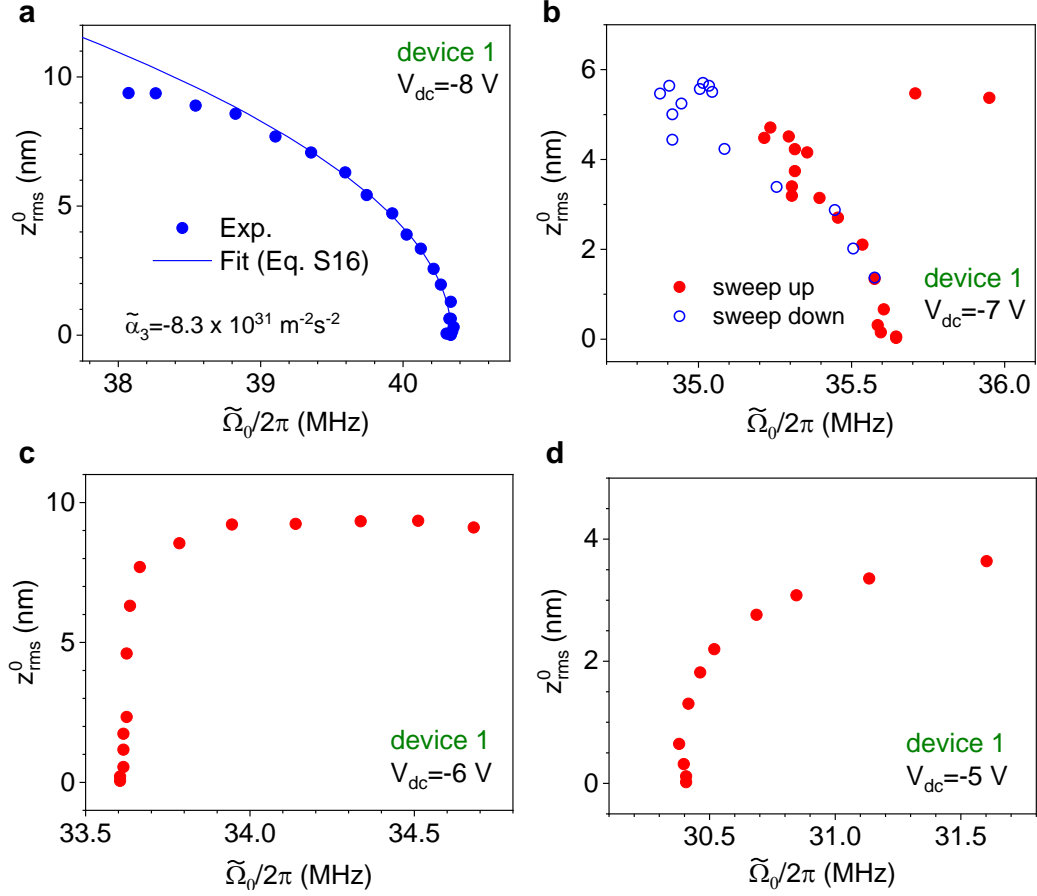


FIG. S11. **Mechanical non-linearities in graphene drums (2)**. Backbone curves (Sec. S6) recorded at four distinct gate biases V_{dc} on device 1. At $V_{dc} = -8 \text{ V}$, a fit using Eq. (S16) allows to extract the non-linear coefficient $\tilde{\alpha}_3$ in Eq. (S15). The data at $V_{dc} = -8 \text{ V}$ and $V_{dc} = -6 \text{ V}$ are plotted in Fig. 2f and 3d, respectively.

S7. EFFECTS OF LASER-INDUCED HEATING.

In our measurements, the laser spot is typically around $1.2 \mu\text{m}$ in diameter⁴¹ and the laser power was set to $P_{\text{laser}} \sim 500 \mu\text{W}$ for the measurements in Fig. 1-3 and $P_{\text{laser}} \sim 200 \mu\text{W}$ for the measurements in Fig. 4. These values corresponds to a reasonable trade off to obtain a sufficiently large Raman signal without being perturbed by softening of the Raman modes due to laser-induced heating⁷⁴. However, the photon flux on the suspended drum is sufficient to induce photothermal effects on its mechanical susceptibility¹⁰. As shown in Fig. S12, at $V_{\text{dc}} = -6 \text{ V}$ the resonance frequency $\Omega_0/2\pi \approx 30.6 \text{ MHz}$ is nearly independent on the laser power below a threshold $P_{\text{laser}} \approx 200 \mu\text{W}$, above which a linear increase in Ω_0 is found, as in previous reports¹⁰. To estimate the temperature (T) increase caused by laser heating, we extracted the thermally induced strain ε_T from the experimental data in Fig. S12a using Eq. (S11).

$$\varepsilon_T = \frac{1 - \nu^2}{E_{1\text{LG}}} \cdot 0.69\pi^2 f(T)^2 \sigma a^2. \quad (\text{S17})$$

As shown in Fig. S12b, the obtained values of ε_T increase linearly with P_{laser} . Using a thermal expansion coefficient $\kappa_T \sim -8 \times 10^{-6} \text{ K}^{-1}$ (Ref. 75), we estimate a temperature increase $\Delta T = -\varepsilon_T/\kappa_T \approx 3 \text{ K}$ at $P_{\text{laser}} = 500 \mu\text{W}$, a value that is about two orders of magnitude too small to account for the dynamical Raman frequency softenings discussed in the main text.

To further rule out laser-induced Raman frequency softening, we repeated the Raman measurements in driven graphene drums at $P_{\text{laser}} = 200 \mu\text{W}$, a value that is low enough to neglect photothermal effects on the mechanical resonance frequency (Fig. S12a,c). Fig. S12d shows the Raman 2D-mode spectra recorded under $V_{\text{dc}} = -6\text{V}$ and $V_{\text{ac}} = 125 \text{ mV}$ at near-resonant and off-resonant drive frequencies. Raman frequency softening under resonant driving akin to Fig. 3 of the main text is clearly observed.

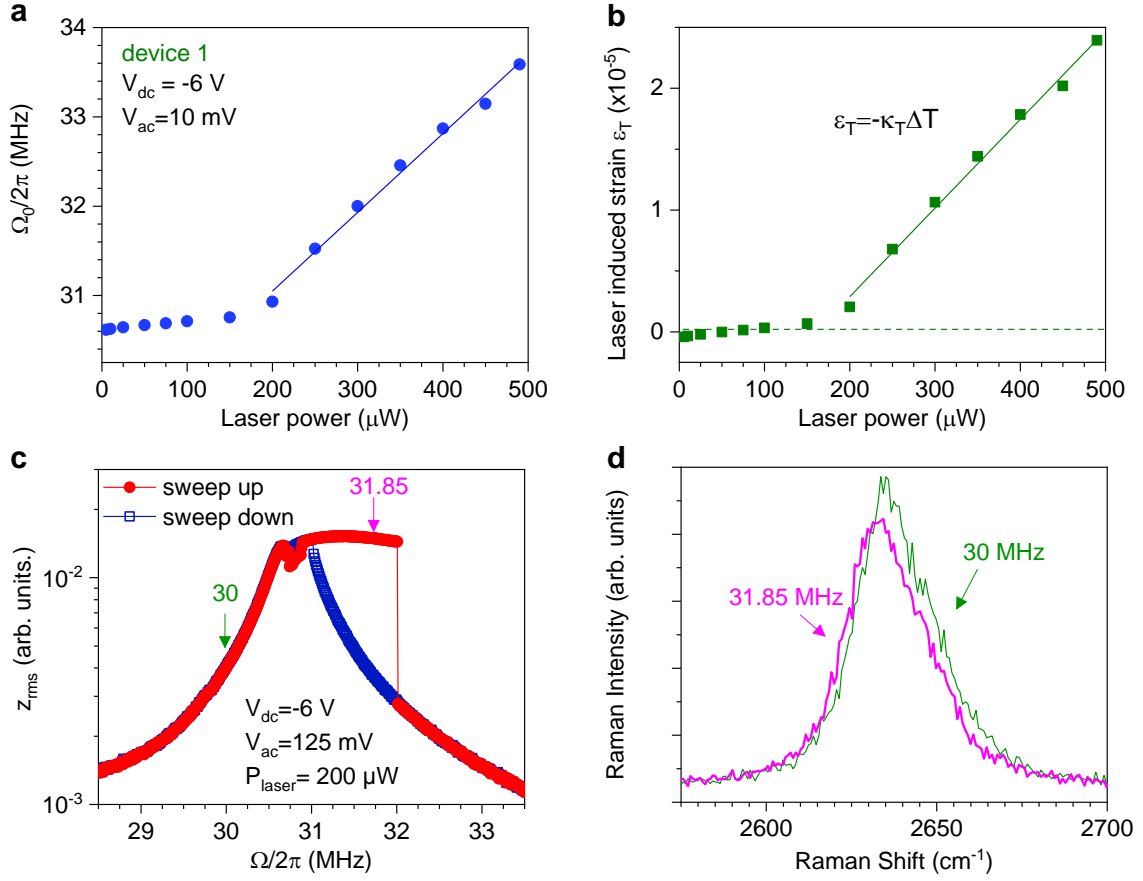


FIG. S12. **Effects of laser-induced heating on the mechanical response of graphene drums.** **a**, Resonance frequency $\Omega_0/2\pi$ measured as a function of the laser power in device 1. The blue line is a linear fit. **b**, Extracted stain (ε_T) as a function of laser power. The solid line is a linear fit (Sec. S7). **c**, Frequency-dependent RMS displacement z_{rms} at $V_{dc} = -6$ V and $V_{ac} = 150$ mV using a laser power $200 \mu\text{W}$. **d**, Two dynamical Raman spectra recorded in the aforementioned conditions under two distinct drive frequencies indicated by the green and pink arrows in (c).

S8. SUPPLEMENTARY DATA ON DEVICE 1

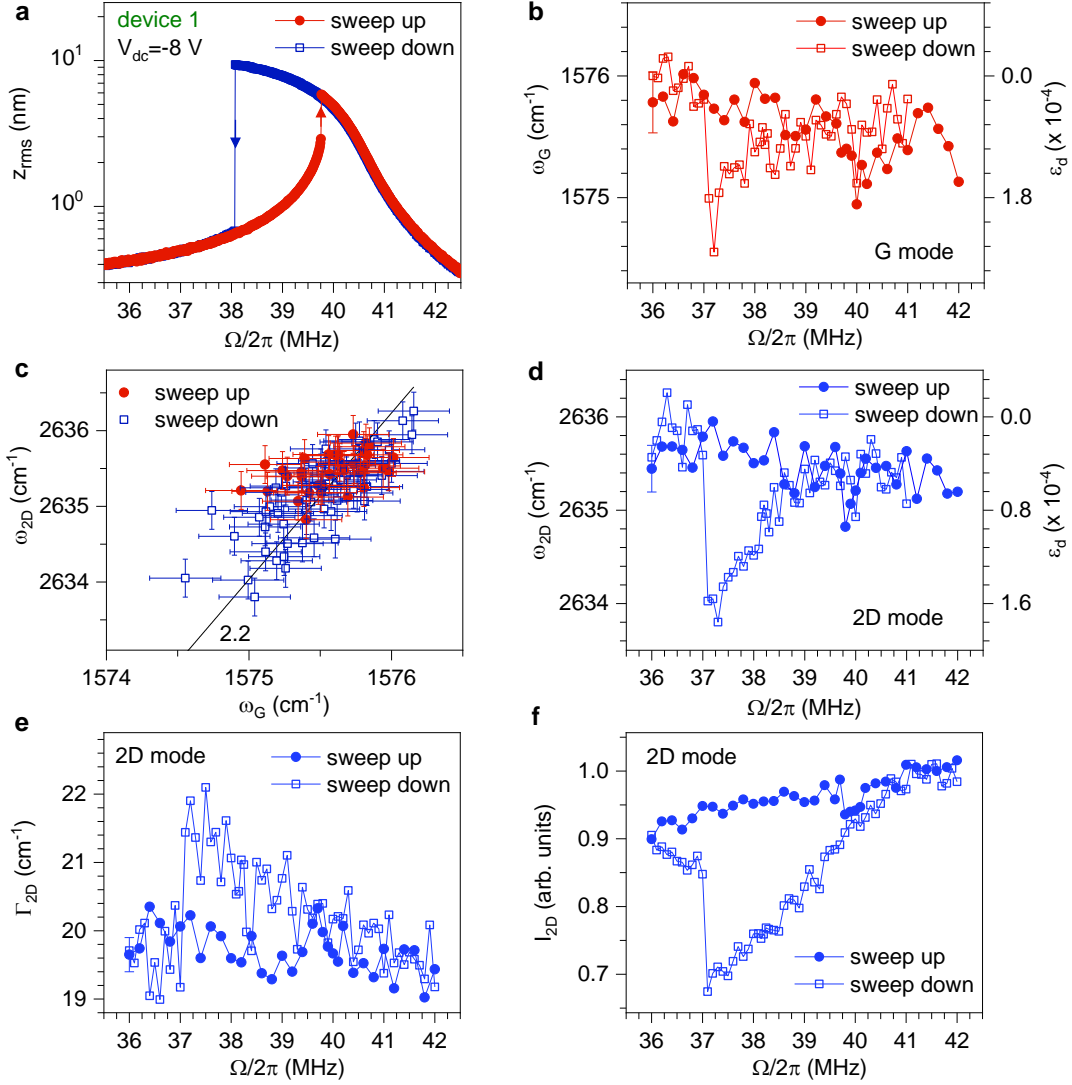


FIG. S13. **Frequency-dependent dynamically-induced strain at $V_{dc} = -8$ V in device 1.** **a**, Frequency-response curves measured on device 1 at $V_{dc} = -8$ V and $V_{ac} = 150$ mV. The arrows denote the jump-up and jump-down frequencies. Frequencies of the Raman G mode (**b**) and 2D mode (**d**) as a function of $\Omega/2\pi$. **c**, Correlations between G- and 2D-mode frequencies. A straight black line with slope of 2.2 is a guide to the eye showing the expected correlation in the case of strain-induced phonon softening³¹. Full width at half maximum (FWHM) (**e**) and integrated Raman intensity (**f**) of the 2D-mode feature as a function of $\Omega/2\pi$. Only one error bar is included in (**b,d,e**) for clarity. The jump frequencies appear at drive frequencies that are slightly redshifted by ~ 1 MHz relative to the frequency-response curves in (**a**). This effect is attributed to photothermally induced mechanical frequency downshift (Sec. S7 and Fig. S12).

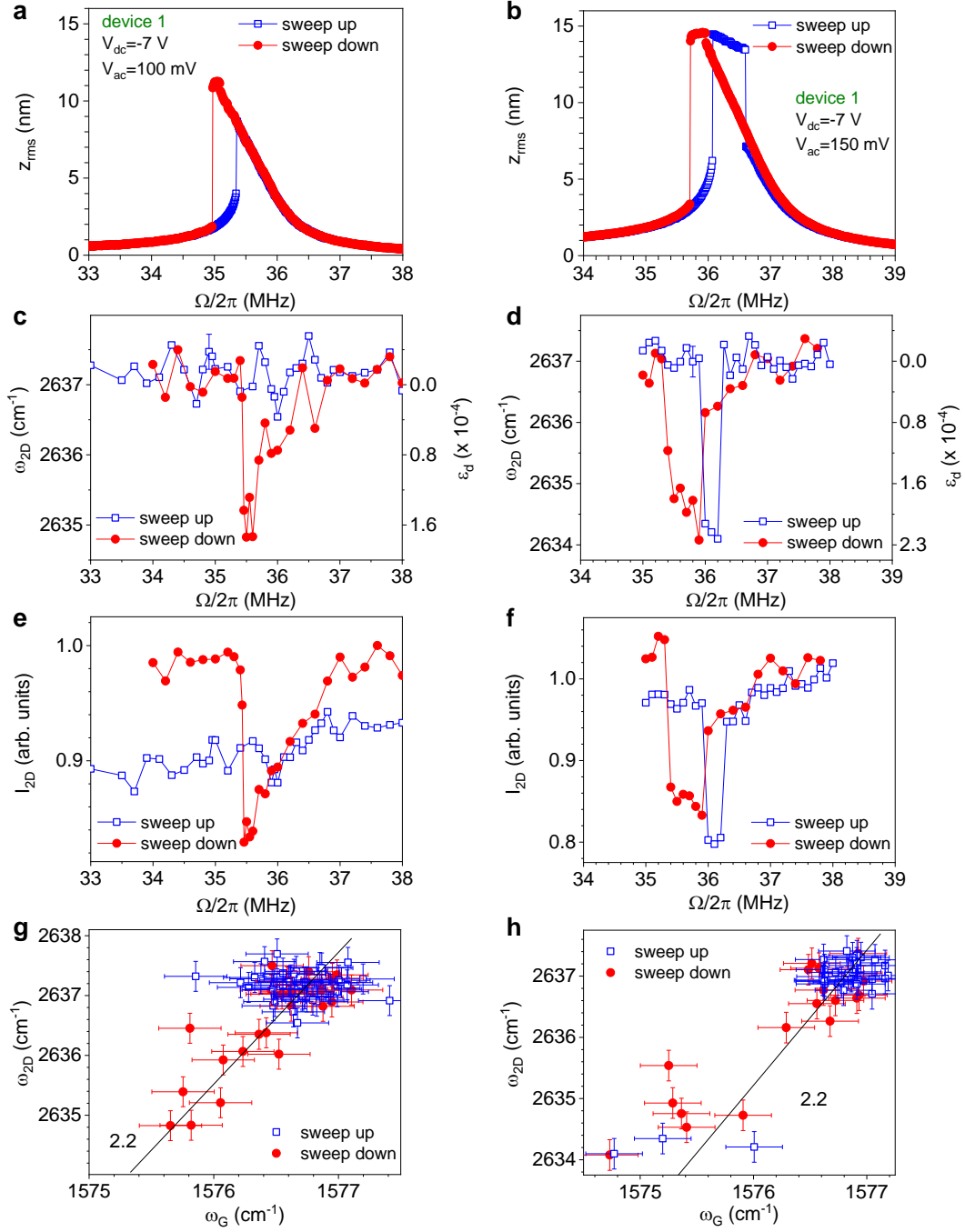


FIG. S14. **Frequency-dependent dynamically-induced strain at $V_{dc} = -7$ V in device 1.** Frequency-response curves measured on device 1 at $V_{dc} = -7$ V with $V_{ac} = 100$ mV (a) and $V_{ac} = 150$ mV (b). Raman 2D mode frequency ω_{2D} (c) and integrated intensity I_{2D} (e) as a function of $\Omega/2\pi$ under $V_{ac} = 100$ mV. (d,f) and $V_{ac} = 150$ mV (c,e). The jump frequencies appear at drive frequencies that are slightly redshifted by $\lesssim 1$ MHz relative to the frequency-response curves in (a). This effect is attributed to photothermally induced mechanical frequency downshift (Sec. S7 and Fig. S12). f, Correlation between the G- and 2D-mode frequencies. The straight black line with a slope of 2.2 is a guide to the eye showing the expected correlation for strain-induced phonon softening.

S9. SUPPLEMENTARY DATA ON DEVICE 2

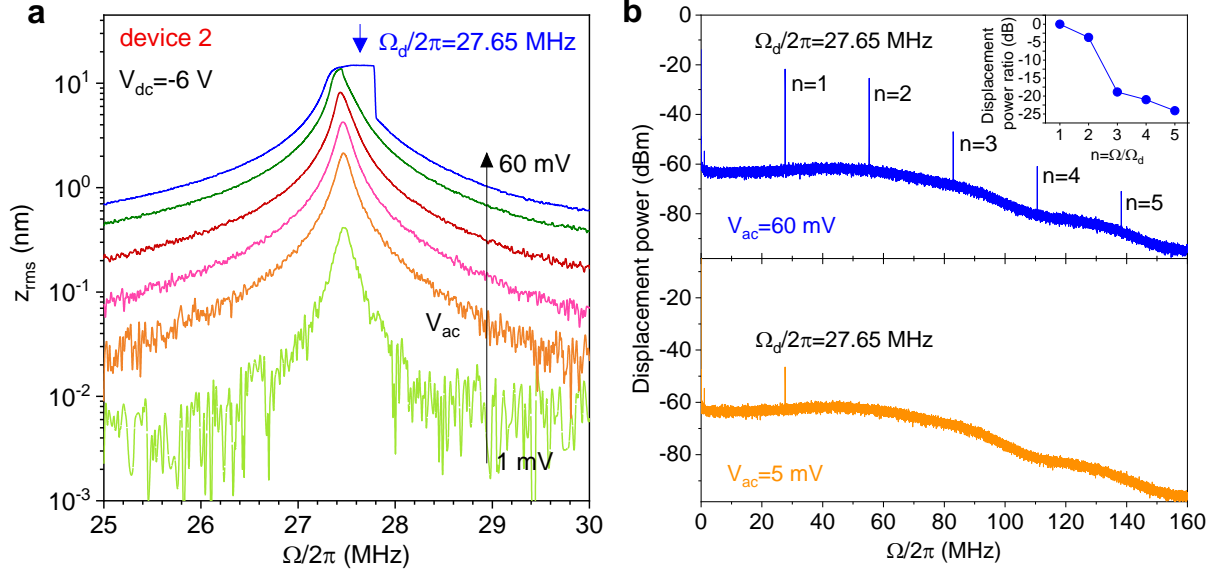


FIG. S15. **Harmonic generation under non-linear mechanical driving.** **a** Frequency-response curve measured at $V_{dc} = -6$ V with V_{ac} ranging from 5 mV up to 60 mV in device 2, a graphene drum similar to devices 1 and 2. The blue arrow denotes the drive frequency $\Omega_d/2\pi$ used in (b). **b**, Broadband displacement power spectral density under $\Omega_d/2\pi = 27.65$ MHz. Bottom panel, with $V_{ac} = 5$ mV; top panel, with $V_{ac} = 60$ mV. Sizeable high-order harmonic components (here up to $5 \Omega_d/2\pi$) are revealed when the drum is resonantly driven with large amplitude. The 50 MHz bandwidth of our avalanche photodiode is clearly visible. Inset: Displacement power of the harmonics relative to the displacement power at Ω_d .

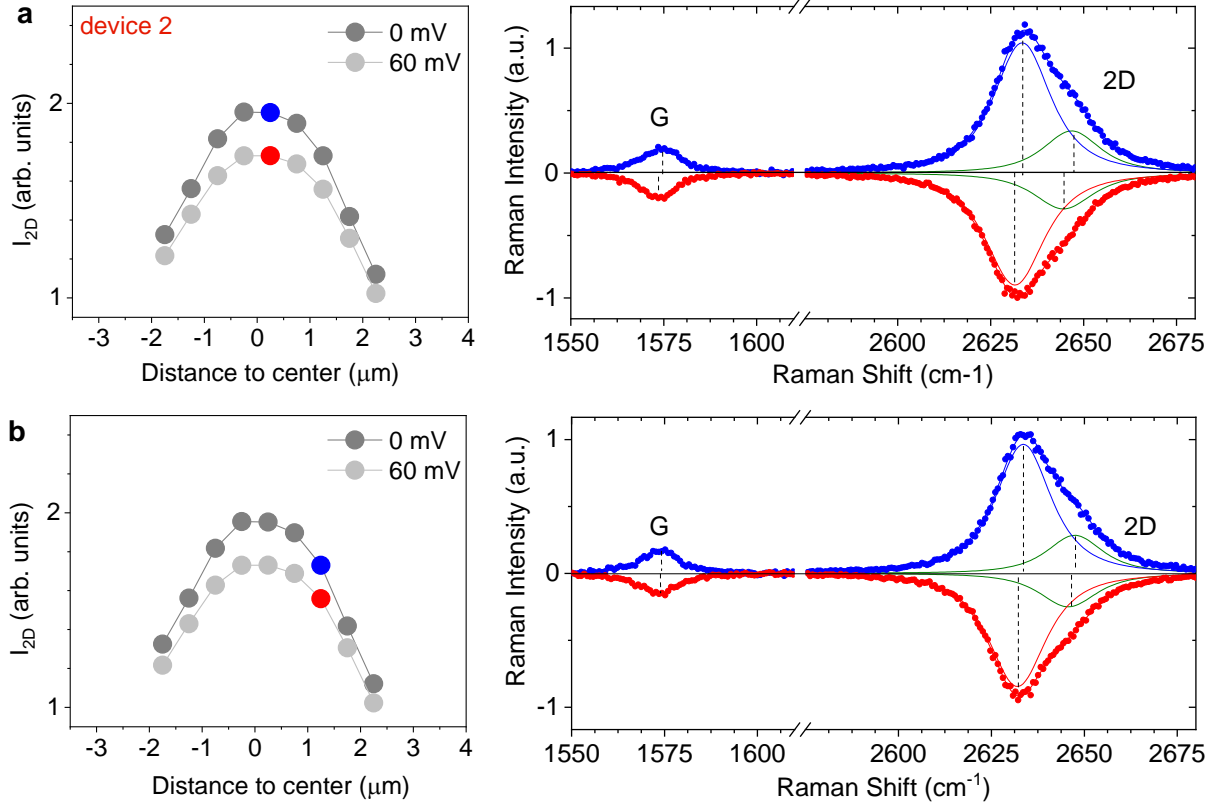


FIG. S16. **Spatially-resolved Raman spectroscopy in device 2.** Selected Raman spectra taken at the centre of device 2 (a) and $2 \mu\text{m}$ away from the centre (b) under $V_{\text{dc}} = -6 \text{ V}$ and $V_{\text{ac}} = 0$ (data in blue) and $V_{\text{dc}} = -6 \text{ V}$ and $V_{\text{ac}} = 60 \text{ mV}$ (data in red). See also Figure 4 in the main text and related discussion.

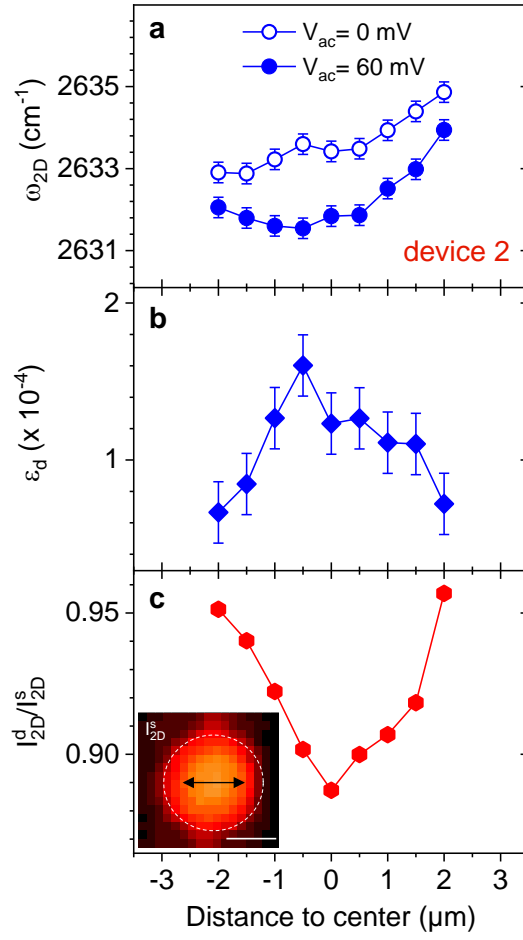


FIG. S17. **Spatially-revolved dynamically-induced strain in device 2.** **a**, Frequency of the Raman 2D mode along the cross-sections highlighted in **c** in a graphene drum (device 2, radius 3 μm) at $V_{dc} = -6$ V and $V_{ac} = 0$ mV (open symbols) and $V_{ac} = 60$ mV (full symbols). **b**, Dynamical strain ϵ_d obtained from the difference of the data in **a**. **c**, Ratio of the Raman 2D-mode intensity in the driven (I_{2D}^d) and static (I_{2D}^s) cases. Inset: Map of the Raman 2D-mode intensity I_{2D}^s recorded on the graphene drum (see white dashed contour), at $V_{dc} = -6$ V and $V_{ac} = 0$ V. The double arrow indicates the location of the line scan. The scale bar is 3 μm . See also Figure 4 in the main text and related discussion.

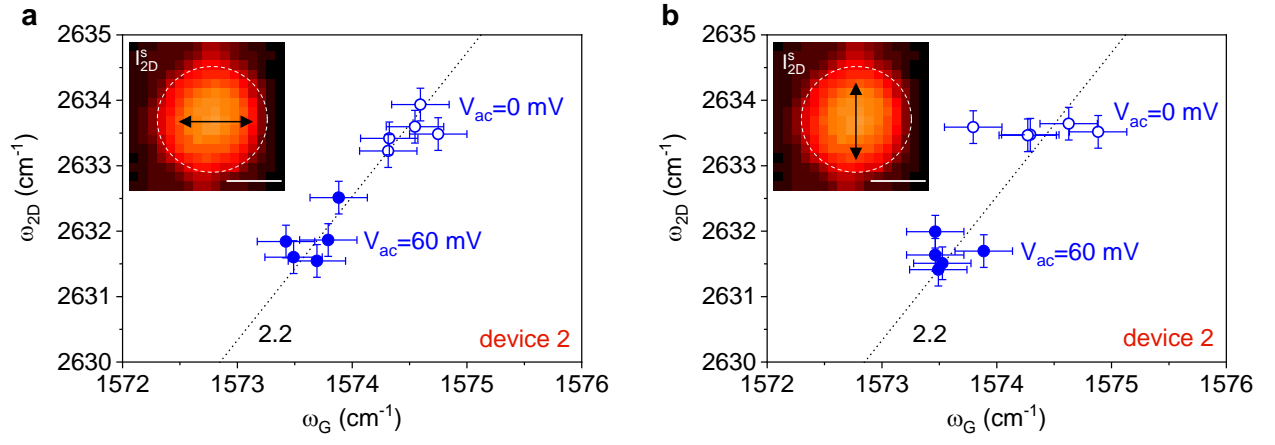


FIG. S18. Correlation plot of the frequencies of the G-mode and 2D-mode frequencies in device 2. The plots in **a** and **b** are made from the data in Fig. S17 and in Fig. 4, respectively. The dashed lines with a slope of 2.2 are guides to the eye showing the expected correlation in the case of strain-induced phonon softening. See also Figure 4 in the main text and related discussion.

S10. SUPPLEMENTARY DATA ON DEVICE 3

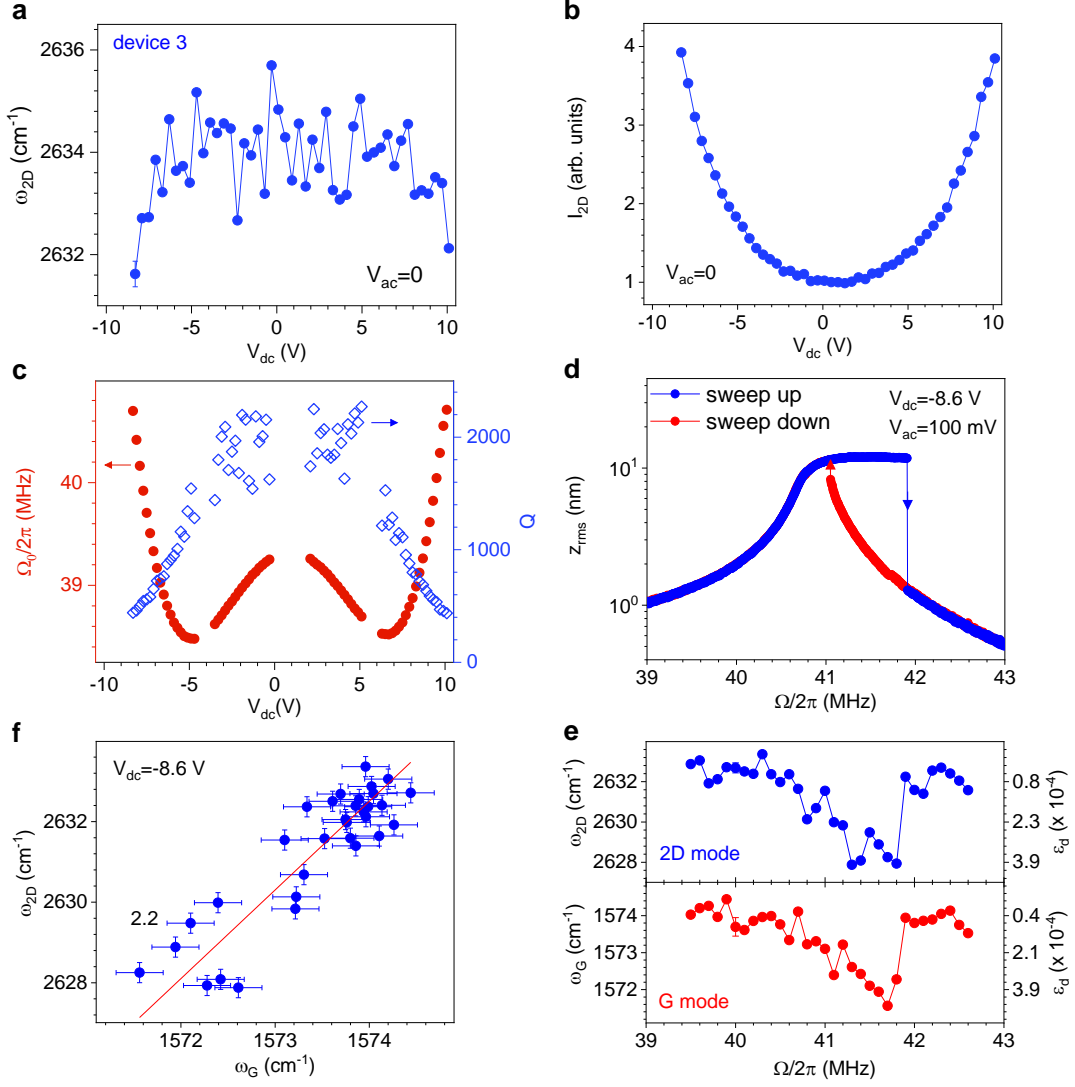


FIG. S19. **Dynamically-induced strain in device 3.** **a,b**, Frequency and Raman intensity of the 2D mode as a function of V_{dc} with $V_{ac} = 0$ for another graphene drum (device 2). This device exhibits larger built in-tension ($\varepsilon_0 \approx 0.014\%$, estimated from Eq. (S12)) and thus reduced gate-tunability as compared to device 1. The limited tunability ($\sim 5\%$ over the range of V_{dc} explored here) is due to a negative spring effect that competes with the gate-induced tension, leading to a “W-shaped” characteristics^{5,8,42}. **c**, Mechanical frequency and corresponding Q -factor as a function of V_{dc} . **d**, Frequency-response curves at $V_{dc} = -8.6$ V with $V_{ac} = 100$ mV. **e**, Corresponding dynamically-induced G- and 2D-mode downshifts and estimated dynamical strain ε_d . **f**, Correlation between the G- and 2D-mode frequencies. The straight black line with a slope of 2.2 is a guide to the eye showing the expected correlation for strain-induced phonon softening.

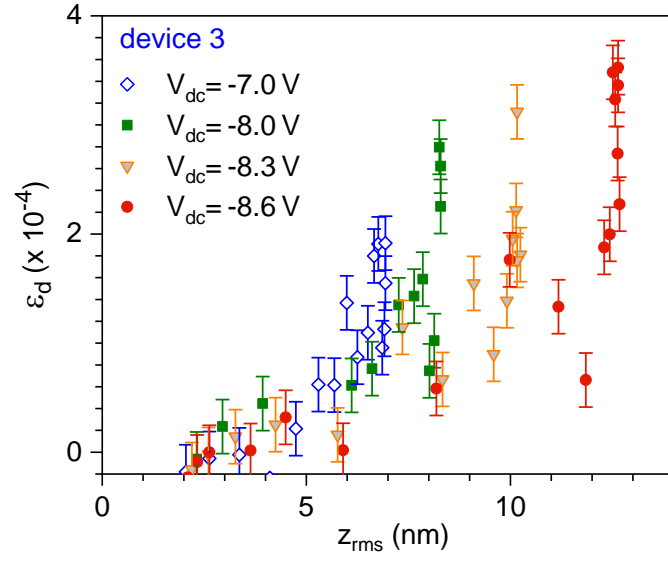


FIG. S20. **Gate-bias dependent dynamically-induced strain ϵ_d measured in device 3.** ϵ_d is obtained from the 2D-mode softening recorded during frequency sweeps (akin to Fig. S19 and Fig. 3) and plotted as a function of z_{rms} , for $V_{\text{dc}} = -7$ V, -8.0 V, -8.3 V and -8.6 V. The error bars come from the standard deviation of the fits of the Raman spectra.